Research Report 2015–02

Regional precipitation extremes over the Maritime Continent

Hongwei Yang

APCC
APEC CLIMATE CENTER

Research Report 2015–02

Regional precipitation extremes over the Maritime Continent

Hongwei Yang

APCC
APEC CLIMATE CENTER

PREFACE

In order to develop adaptation and mitigation strategies, both global and local scale information on climate change is necessary in order to assess the impacts of changes in human life and the natural environment. The COordinated Regional climate Downscaling EXperiment (CORDEX) was established to address that need. The World Climate Research Programme sponsored CORDEX to organize an international coordinated framework to produce an improved generation of regional climate change projections world-wide. These improved projections are to be used as inputs into impact and adaptation studies within Fifth Assessment Report of the Intergovernmental Panel on Climate Change timeline and beyond. CORDEX will produce an ensemble of multiple dynamical and statistical downscaling models considering multiple forcing global climate model from the Coupled Model Intercomparison Project Phase 5 archive. Multiple common domains covering all (or most) land areas in the world have been selected.

The Asia-Pacific Network, along with seven countries (Indonesia, Malaysia, Philippines, Thailand, Vietnam, Cambodia, and Lao PDR), developed and has funded the Southeast Asia Climate Downscaling Experiment (SEACLID) project for three years, starting from October 2013. Taking advantage of SEACLID, CORDEX-Southeast Asia (SEA) was established with the intentions of providing improved high-resolution climate project information for local hydrological and agriculture sectors. The Asia-Pacific Economic Cooperation (APEC) Climate Center (APCC) later joined the CORDEX -SEA project as one of the institutes from outside the SEA region.

We try to provide change information of extreme precipitation in this study. This information is essential to analyze the potential climatic impacts and adaptation measurements for extreme climate events. Thus, the hindcast and historical downscaling experiments for current climate were forced by reanalysis data and global model output in this study, respectively. Two climate change downscaling processes were driven by global model projections.

I hope that the results and data outputs of this study can provide improved high resolution climate information for the hydrological and agriculture sectors, which might eventually support the building of a long-term warning system. End-users and policy-makers will be able to weigh their response options based on these reliable local scale projections.

APCC will continue to promote the best use of our research outcomes in various scientific and application areas. Our successes and achievements would not have been possible without the support of our valued partners. Beside my appreciation to the APCC researchers, I extend my thanks to you and I hope you enjoy this research report.

Dr. **Chin-Seung Chung**, Director
APEC Climate Center
January 2016

ABSTRACT

The total amount and frequency of extreme precipitation were analyzed over the Maritime Continent with data from observations, dynamic downscaling of a hindcast experiment forced by the European Centre for Medium-Range Weather Forecasts Reanalysis-Interim dataset, a historical experiment forced by the Hadley Centre Global Environmental Model Version 2-Atmosphere-Ocean (HadGEM2-AO) global coupled model, as well as near future projections from a Representative Concentration Pathway (RCP) 4.5 experiment and far future projection from a RCP 8.5 experiment forced by the future projections of HadGEM2-AO output.

Correlations between observed extreme precipitation and the El Nino Southern Oscillation (ENSO) as well as the Madden-Julian Oscillation (MJO) during the rainy season were quantified over the local lands. We found that the impact of ENSO on extremes is dependent on the MJO phases. ENSO impacts extremes by changing the interannual variation component, while MJO influences the extremes through both the annual cycle and the intraseasonal component of the extreme itself.

The hindcast experiment reasonably simulated the climate's annual cycle of rainfall and extremes. Qualitatively, the impacts of ENSO and MJO on the extremes were correctly reproduced in the hindcast experiment. However, the impact was weaker than that in the observational study. Variation of extremes as a function of ENSO and MJO was generally comparable with the observations, except that the magnitude and spread of the extremes were generally overestimated.

The historical experiment data were capable of representing the annual cycle of rainfall and extremes, but the links between extreme precipitation and ENSO or MJO were not very clear. Nevertheless, the historical experiment generally had larger biases for the extremes than those in the hindcast experiment.

There was no clear trend in the changes of the mean extremes in the future. However, the daily variability of extremes showed an increasing trend over most lands. Over the northern the Indo–China Peninsula (IC), southern IC, Borneo, and Java, large extreme rainfall events will likely become frequent in the future. In contrast, less large extreme rainfall events are forecasted for Luzon and Visayas. No large changes are forecasted over New Guinea. Lastly, Sumatra and Mindanao showed uncertain changes in the future.

CONTENTS

1. Introduction

The COordinated Regional climate Downscaling EXperiment (CORDEX) was established to improve the coordination of international efforts in regard to regional climate downscaling (RCD) research. The sophisticated circulation and thermodynamics forcing over the Maritime Continent create many difficulties for hydrological and agriculture management. Thus, the CORDEX-Southeast Asia (SEA) project was established recently over the Maritime Continent with the aim of providing improved high-resolution climate project information for hydrological studies and the agriculture sector.

The Maritime Continent is composed of thousands of islands, among which the Indo-China Peninsula (IC), Sumatra, Borneo, Java, New Guinea, and the Philippines represent extensive lands with large populations and economies. The water resources sector relies highly on estimations of precipitation. Future projections from global models predict that the mean precipitation will likely change significantly in this region by the end of the 21st century (Solomon et al., 2007).

Yang (2013, 2014) carried out dynamic downscaling research over the Maritime Continent at both 50 and 25 km spatial resolutions. The experiment employing the 25 km grid outperformed the experiment employing the 50 km grid in many aspects such as added values, spatial and temporal correlations, and root mean square errors. However, extreme climate events were not studied in the improved experiments because of limited resources.

Extreme precipitation is especially important because this high order statistic quantity is associated with large uncertainty and can severely impact the environment and the economy. For example, during late 2006 and early 2007, the worst flooding in a century over southern Peninsular Malaysia was caused by heavy precipitation associated with strong northeasterly winds over the South China Sea (Tangang et al., 2008). Extreme rainfall means the occurrence of precipitation above a threshold value (e.g., 90th percentile) near the upper end of the range of precipitation.

Changes in the tropical water cycle are dominated by periodic warming and wetter conditions associated with the El Nino Southern Oscillation (ENSO) (Allan and Soden,

2008). The tropical rainfall pattern shifts east during the El Nino phase (Rasmusson and Carpenter, 1982; Rasmusson and Wallace, 1983). Extreme precipitation over IC, the Philippines, and the northern tip of Borneo responds significantly to ENSO phases. However, Sumatra, Java, Guinean, and most parts of Borneo do not show such significant interannual changes in extremes corresponding to ENSO phases (Kenyon and Hegerl, 2010). In comparison, Alexander et al. (2009) found that except for the northern tip of Borneo, extreme precipitation does not significantly increase during strong La Nina relative to strong El Nino phases over IC, Sumatra, and the Philippines. The impacts of ENSO and the Madden–Julian Oscillation (MJO) are important topics not only in regard to the downscaling of current climate data but also for future scenarios research.

The MJO is the dominant mode of large–scale tropical intraseasonal variability (Madden and Julian, 1994). Observations show that extreme event frequencies during active MJO periods are significantly higher than those in quiescent MJO phases in locations that are obviously influenced by the MJO (Jones et al., 2004).

A few observational studies have showed increasing trends of extreme precipitation over parts of IC and the Philippines (Westra et al., 2013), whereas Kenyon and Hegerl (2010) showed moderate decreases of extreme precipitation over SEA. Nevertheless, links of extreme precipitation to large–scale circulation modes over the Maritime Continent have been studied less intensively than those over other regions, especially in the dynamic downscaling community.

In this study, we were motived to detect the impacts of ENSO and MJO on the extreme precipitation over the Maritime Continent by analyzing the observation data first. Then, the relationships between simulated extreme precipitation and observed ENSO and MJO were investigated. The probability distribution of extreme precipitation is discussed herein.

The entire report is organized as follows: we introduce the data that were used in Section 2. The regional model and corresponding experimental design are described in Section 3 and 4, respectively. Section 5 contains the results from the observations and hindcast, historical, and future projection experiments. The discussions and conclusion are presented in Section 6.

2. Data

Satellite rainfall from the Climate Prediction Center Morphing Technique (CMORPH) (Joyce et al., 2004) and reanalysis rainfall from the Asian Precipitation–Highly Resolved Observational Data Integration Towards Evaluation of Water Resources (APHRODITE) project (Yatagai et al., 2012) were used to analyze the observed extreme events.

To investigate the influence of ENSO and MJO on extreme precipitation over SEA, both the ENSO and MJO index were applied. The Oceanic Nino Index (ONI) constructed from National Oceanic and Atmospheric Administration (NOAA) extended reconstructed sea surface temperature (SST) data (Huang et al., 2014) was used to measure the El Nino and La Nina events. The NOAA interpolated outgoing longwave radiation (OLR) (Liebmann and Smith, 1996) and zonal winds at 200 and 850 hPa from the National Centers for Environmental Prediction (NCEP) reanalysis II (Kanamitsu et al., 2002) were used to construct the MJO index according to Wheeler and Hendon (2004). Horizontal winds at 850 hPa and vertical velocity at 500 hPa from NCEP reanalysis II were also used for analyzing the large–scale dynamics.

The European Centre for Medium–Range Weather Forecasts Reanalysis (ERA)–Interim (Dee et al., 2011) reanalysis dataset was used as the large–scale forcing fields for the hindcast experiment. The output of the Hadley Centre Global Environmental Model Version 2–Atmosphere–Ocean (HadGEM2–AO) (Baek et al., 2013) global coupled model was used as forcing for the historical (control) experiment and future projection experiments.

3. Model

The Weather Research and Forecast (WRF) 3.5 model, which is a primitive equation limited-area model under sigma coordinates, was used in this study. In general, WRF is a regional prediction and downscaling system designed to meet both operational forecasting and atmospheric research needs. This system has advanced software architecture that allows for parallel computing and system extensibility. The development of state-of-the-art WRF technology was undertaken as a collaborative project by several organizations including the National Center for Atmospheric Research (NCAR), the Forecast Systems Laboratory, NOAA, NCEP, the Air Force Weather Agency (AFWA), the Naval Research Laboratory, the University of Oklahoma, and the Federal Aviation Administration. The WRF model allows researchers to conduct simulations reflecting either real data or idealized configurations and WRF is suitable for many applications at different scales ranging from meters to thousands of kilometers. Such applications include research and operational numerical weather prediction, data assimilation and parameterized physics research, downscaling climate simulations, driving air quality models, atmosphere-ocean coupling, and idealized simulations of phenomenon such as boundary layer eddies, convection, and baroclinic waves. There are two dynamics solvers in the WRF Software Framework, namely, the Advanced Research WRF (ARW) solver (originally referred to as the Eulerian mass or "em" solver), which was developed primarily at NCAR, and the Nonhydrostatic Mesoscale Model solver, which was developed at NCEP. We employed the ARW solver in this study. The governing equations of the ARW dynamics solver are the compressible, nonhydrostatic Euler equations. These equations are written in flux form, and their variables satisfy conservation equations following the philosophy of Ooyama (1990). Further, the equations are expressed by using a terrain-following mass vertical coordinate system (Laprise, 1992). In this model, the top surface is a constant pressure surface; we set this surface at a pressure of 50 hPa. Arakawa C-grid staggering was applied for the horizontal grid. A third order Runge Kutta scheme with a smaller time step for acoustic and gravity-wave modes was applied for time-split integration (Klemp and Wilhelmson, 1978; Skamarock and Klemp, 1992; Wicker and Skamarock, 2002). The WRF model offers multiple physical options that can be combined in any way

(Skamarock et al., 2005).

In this study, we chose the WRF Single-Moment 6-Class Microphysics graupel scheme (Hong et al., 2004) for microphysics parameterization; this scheme includes six types of hydrometeors, namely, water vapor, cloud water, rain, cloud ice, snow, and graupel in six different arrays. Thus, it allows for the existence of supercooled water and a gradual melting of the snow below the melting layer. It introduced a new method for representing mixed-phase particle fall speeds weighted by the mixing ratios for the snow and graupel particles by assigning a single fall speed to both; this fall speed was applied to both sedimentation and accretion processes. We chose the modified Tiedtke scheme (Tiedtke, 1989; Zhang et al., 2011) for cumulus parameterization; this scheme is a mass-flux type scheme that employs a convective available potential energy-removal time scale, a shallow component, and momentum transport. Land surface parameterization follows the unified Noah land-surface model (Tewari et al., 2004), which is a unified NCEP/NCAR/AFWA scheme with soil temperature and moisture in four layers, fractional snow cover, and frozen soil physics. The Yonsei University (Hong et al., 2006) planetary boundary layer was employed here; with this technique, the counter gradient terms were used to represent fluxes due to non-local gradients. The surface layer scheme was the Fifth-Generation Penn State/NCAR Mesoscale Model Monin-Obukhov scheme (Paulson, 1970; Dyer and Hicks, 1970; Webb, 1970; Beljaars, 1994; Zhang and Anthes, 1982), which is based on the Monin-Obukhov scheme with a Carlson-Boland viscous sub-layer and standard similarity functions from look-up tables. The long wave and short wave radiative transfer model followed the Community Atmospheric Model (CAM) scheme (Collins et al., 2004), which is based on the CAM 3 climate model used in the Community Climate System Model; it takes into account the contributions of aerosols and trace gases and uses yearly carbon dioxide, constant nitrous oxide (311E-9), and methane (1714E-9).

The lateral boundary forcing fields included geopotential height, air temperature, specific humidity, and horizontal winds. The width of the buffer zone in our model was set to be 10 grid points, where the prognostic variables of the WRF model were nudged toward the large-scale forcing fields following the method of Davies and Turner (1977) with Newtonian nudging and horizontal diffusion within the

regional climate model (RCM) buffer zones. The initial state conditions were as follows: surface pressure, sea–level pressure, 2–m height moisture, 2–m height temperature, 10–m height horizontal winds, soil moisture, soil temperature, and skin temperature. The skin temperature over the ocean was considered as the SST. We obtained 30′ horizontal resolution topography and land use data for the Noah land surface model from the U.S. Geological Survey. The 30′ soil type data were obtained from the State Soil Geographic Database, and 5″ global data were obtained from the Food and Agriculture Organization of the United Nations.

4. Experimental design

The tropical climate over the Maritime Continent is very important and unique as it is located in the most active convective area of the world and is influenced by both Hadley and Walker circulations. The Maritime Continent consists of more than 10,000 islands with high topography.

To consider the climate system in this region, we needed (1) a sufficiently large domain size so that the regional model could develop its own dynamics and (2) sufficient computational resources; we designed our model domain covering the Maritime Continent region to extend from 15°S to 27°N and from 90°N to 145°E (Fig. 1). We chose the cylindrical equidistant map projection, as the grid is close to rectangular in Euclid space over the tropical region. The zonal and meridional grid space was chosen as approximately 0.25° in order to adapt to the mesh resolution of observed data that were available for our study. The model had 221 west–east and 169 south–north grid points, 37 sigma layers were used in the vertical direction up to 50 hPa.

Four experiments named as the hindcast experiment, historical experiment, Down–45, and Down–85 were designed, and these experiments were initiated and forced by the ERA–Interim, HadGEM2–AO historical run, HadGEM2–AO Representative Concentration Pathway (RCP) 4.5, and HadGEM2–AO RCP 8.5 future projections, respectively. The prescribed SST was from the same dataset of the lateral boundary forcing for each experiment. Here, the prefix “Down” in the experimental names refers to downscaling. The historical experiment was used as our control experiment, and its output was used as reference data to assess the climate change. The ERA–Interim data are available at 6–h intervals with a horizontal resolution of 0.75° and 37 pressure levels. The output of HadGEM2–AO consists of 6–hourly data with a horizontal resolution of 1.25° in terms of the latitude and 1.875° in terms of the longitude. The enhanced greenhouse conditions were prescribed both in lateral boundary conditions and inside of the model domain in Down–45 and Down–85. The physical parameterization scheme and model configuration were kept the same for all experiments. All model parameters were considered with their default values without tuning.

The hindcast experiment was run from 1 January 1980 to 31 December 2005. The historical experiment was run from 1 January 1970 to 31 December 2005. Down–45 and Down–85 were run from 1 January 2006 to 31 December 2100. The model outputs of the hindcast and historical experiments from 1981 to 2005 were analyzed. The near and far futures were defined as periods from 2021 to 2045 and from 2071 to 2095, respectively. The historical reference data for studying climate change was taken from the period 1981–2005, a sub–period of the historical experiment.

5. Results

5.1 Observational analysis

In order to verify the ability of the WRF model to simulate extreme rainfall events over the Maritime Continent, we first investigated the correlations between extreme precipitation and large–scale circulation patterns of ENSO and MJO in the observational dataset.

Satellite rainfall from CMORPH consisting of an half hourly dataset sits on an 8 km grid, and data are available since 1998 (Joyce et al., 2004). AghaKouchak et al. (2011) showed that CMORPH is capable of detecting extreme precipitation events. Before 1998, the gage recode of observed precipitation over most of the SEA region was generally poor in that either the recode was short or it had no regularity in terms of the missing data, except over IC and the Philippines (Westra et al., 2013). Fortunately, the APHRODITE project has gathered pre–1998 data from individual collections, precompiled datasets, and the Global Telecommunication System (0.25° × 0.25° and daily; Yatagai et al., 2012). Fig. 2 shows the climatology of concatenated daily rainfall of APHRODITE (1979–1997) and CMORPH (1998–2013), and the results clearly show the rainfall peaks that likely contributed to the extreme events. Through empirical orthogonal function (EOF) analysis over individual land in IC, Sumatra, Java, Borneo, New Guinea, and the Philippines, an inhomogeneous rainfall anomalous pattern was found only over IC and the Philippines. To avoid smoothing of extreme rainfall due to averaging over opposite anomaly patterns of rainfall, IC was further divided into northern IC and southern IC, and the Philippines was further divided into Luzon and Visayas (LV) and Mindanao (Fig. 1), according to the different spatial patterns of the leading EOF. By using the EOF analysis again over northern IC, southern IC, LV, and Mindanao, this confined the homogeneous anomaly patterns in the individual regions, just like in the cases over Sumatra, Java, Borneo, and New Guinea (Fig. 3). The consistent peaks in climate–related rainfall (Fig. 2) and the leading EOF pattern over individual regions (Fig. 3) confirmed that the separation of rainfall domains was reasonable to investigate the extreme precipitation. Therefore, over these eight regions, the areal mean of the concatenated daily rainfall derived through application of the quantile mapping technique on the

time series was analyzed to find the links between extreme events and large-scale circulation patterns of ENSO and MJO.

The base period for extreme events was 30 years from 1980 to 2010. The 90th percentile of daily precipitation during the base period was selected to distinguish extreme and normal rainfall. Two indexes for extreme totals and extreme frequencies were generated for each of the eight lands without removing the seasonal cycle of rainfall. By keeping the annual cycle, the indexes reflect the wettest events that mainly fell in the rainy season during the entire period. From a practical viewpoint, these indexes represent the extreme events that have the greatest impact on the environment and society (Manton et al., 2001).

Let r denote daily rainfall; r_i is the rainfall amount on the ith day; def denotes the daily extreme frequency; det is the daily extreme total; and wet and met denote weekly and monthly extreme totals, respectively. Then,

$$def_i = \begin{cases} 1, r_i > threshold \\ 0, r_i \le threshold \end{cases}$$

$$det_i = \begin{cases} r_i, r_i > threshold \\ 0, r_i \le threshold \end{cases}$$

where the $threshold$ is the 90th percentile of daily rainfall.

$$wet_j = \sum_{\text{day } i\ (1\sim 7) \text{ in week } j} det_i$$

$$met_j = \sum_{\text{day } i \text{ in month } j} det_i$$

The weekly and monthly totals of extreme precipitation were both defined because we wanted to find the precursors of extreme events that might relate to low-frequency tropical intraseasonal variations and interannual variabilities.

To make sure our analysis focused only on the rainy season, the monthly climatological annual cycle of total rainfall, extreme totals, and extreme frequencies were investigated to determine the rainy season (Fig. 4).

As shown in Fig. 4, the rainy season of the typical boreal monsoon climate clearly occurred in May-September (MJJAS) over northern IC where the monsoons

began in May, matured in July–August, and retreated in October. The peaks of extremes were very consistent with the seasonal cycle of rainfall. Coincident with the reversal of monsoon flow over southern IC, the rainy season there took place at the beginning of low-level north-easterly monsoon flow, and it was very short, i.e., lasting only from November to December; this period contributed the most to the extreme events. There was another weak rainfall peak around May, but we did not consider it as part of the rainy season because it did not contribute to the extreme rainfall. Over Sumatra, the rainfall system and extreme events both consistently showed double peaks during October to April when the onshore wind along the western coast was westerly (Wang, 2006). Rainfall and extremes over Java were fairly consistent in their seasonal phase and commencement during the wet season that lasted from November to March; here, the rains were due to the developing and enhanced local north-westerly winds resulting from upstream north-easterly monsoon flow that crossed the equator following the conservation of potential vorticity. Over Borneo, the rainy season lasted from October to May and showed decreasing tendencies in terms of both rainfall and extreme rainfall when the north-easterly monsoon winds reached the equator region as the season advanced and enhanced the low-level, quasistationary Borneo vortices (Cheang, 1977; Chang et al., 2003; Tangang et al., 2008). Over New Guinea, the rainy season took place from December to May. The north-easterly monsoon flow that crossed the equator turned north-westerly in December and brought plenty of moisture from the north-west Pacific; in this region, the moisture encounters high topography. Extreme rainfall had the same phase as the rainfall itself. Over LV, the rainy season took place from June to December. In mid-June, the boreal summer monsoon rains burst in the vicinity of the Philippines and retreated during August and September. From October to December, high rainfall was due to the onshore north-easterly monsoon winds from the north-west Pacific. The extreme rainfall had the same phase. Over Mindanao, the annual rainfall was fairly evenly distributed throughout the whole year. However, during June to January, the rainfall and especially the extreme rainfall were higher than those in other months; thus, this period was selected as the rainy season. Typhoons frequently invaded the Philippines during the rainy season and were an important driving factor of the extreme rainfall.

The order of the rainy season from north to south followed a smooth transition of the heating source from the Asian summer to Asian winter monsoon (Lau and Chan, 1983; Meehl, 1987; Tanaka, 1994). The seasonal cycle of rainfall here is largely dominated by interactions between the complex terrain and the annual reversal of the surface monsoonal winds (Chang et al., 2005).

To find the link between extreme events and ENSO, the monthly extended reconstructed SST anomaly from NOAA was used to construct ONI by calculating the time series over the Nino 3.4 region (5N–5S, 170–120W). El Nino (La Nina) is characterized by five consecutive 3–month running mean SST anomalies in the Nino 3.4 region that are above (below) the threshold of +0.5°C (-0.5°C).

Since the atmospheric response can lag El Nino by several months (e.g., Hegerl and Wallace, 2002; Kenyon and Hegerl, 2010), we attempted to study the lead–lag connection between the extreme totals and ENSO. We selected the monthly extreme totals in the rainy season and the corresponding ONI in the lead–lag months for this purpose.

Since the ONI essentially reflects important interannual variation of the large–scale circulation mode, we were motivated to focus on the link between the interannual component of extreme events and ONI by dividing the rainfall into the climatological annual cycle ($rainAC$), interannual variation ($rainIA$), intraseasonal variation ($rainIS$), and synoptic disturbances ($rainSY$) (Yang and Wang, 2015). The decomposition of rainfall was conducted as follows. First, the $rainAC$ was obtained by calculating the 31–day running mean over the climatological daily mean data averaged for the entire period. Second, the daily mean anomaly was obtained by subtracting the $rainAC$ from the daily mean data. The $rainIA$ component was further obtained by calculating the 365–day running mean over the daily mean anomaly data. Finally, the ($rainSY$ + $rainIS$) field was obtained by subtracting the $rainIA$ component from the daily mean anomaly data. The $rainIS$ component was further separated from the $rainSY$ component by calculating the 5–day running mean over the ($rainSY$ + $rainIS$) field.

Table 1 gives the correlation values between the various components of extremes and -ONI. We found that all the correlations between the extreme total of the interannual component and -ONI passed a 90% significant test. The averaged correlation throughout eight lands was 0.40. None of the other components had a such high averaged correlation. The extreme total of the intraseasonal component did not correlate with -ONI at all in terms of the average. While the extreme totals of $rainAC$ and $rainSY$ were correlated with -ONI very weakly in terms of the average, most of them were insignificantly correlated with -ONI over the individual lands. The averaged correlations between the full field of extreme rainfall met and -ONI were as low as 0.09.

Therefore, the impact of ENSO on rainfall extreme totals over Maritime Continent lands was mainly through its influence on the interannual component of extreme rainfall. The impact of ENSO was very weak on the full field of extreme rainfall. Negative SST anomalies in the equatorial Pacific (i.e., La Nina conditions) created favorable conditions for heavy precipitation days over the Maritime Continent lands through slow influence at the interannual timescale. Positive SST anomalies in the equatorial Pacific (i.e., El Nino conditions) impacted the extreme rainfall in the opposite way. However, the local or remote forced variabilities at shorter timescales would likely have nonlinear interactions that would hide the modulation from ENSO.

In fact, many studies have reported that the impact of ENSO on the Maritime Continent monsoon is very weak during the boreal winter season, especially after the Asia winter monsoon is active (McBride and Nicholls, 1983; Holland, 1986). Chang et al. (2004) showed that the strong effect of the wind–terrain interactions over the Maritime Continent plays important role on local interannual variabilities for cold surges, Indian Ocean zonal wind anomalies, and cross–equatorial flow reaching the deep tropics. Another sources of interannual variability is the seasonal variations of MJO activity (Hendon et al., 1999). The relatively lower correlations between the extreme total of the interannual component and -ONI over Sumatra and Java were consistent with the findings of Kenyon and Hegerl (2010). However, in contrast to the previous studies, our analysis gave another explanation of how ENSO modified the rainfall system over the lands in the Maritime Continent region.

To detect the link between extreme events and the MJO, daily NOAA Interpolated

OLR and zonal winds at 200 and 850 hPa from the NCEP reanalysis II dataset were used to construct the MJO index (MJOI) according to Wheeler and Hendon (2004). In contrast to that index, we took an extended domain (-12.5–25N and 0–360E) according to the CORDEX-SEA project for convenience in our WRF downscaling study. The meridional averaging of the OLR and wind fields was skipped before carrying out a multivariate EOF analysis. The localized MJO index (LMJOI) was reconstructed from the two leading principal components (PCs) of the multivariate EOF analysis and the two leading EOF patterns of only the OLR field over each of the eight lands. The MJO life cycle is shown in Fig. 5.

The links between various extreme components and the MJO index are shown in Table 2. Weekly totals of extreme rainfall wet were weakly but significantly correlated with the LMJOI over all lands with an averaged correlation of 0.15. The correlation value was not high because the sample size was large and there were important contributions of extreme events from local synoptic disturbances. The impact of MJO on extreme rainfall mainly resulted from its influence on the intraseasonal component of extreme rainfall. Like the MJO effects on wet, the MJO effects on $wetIS$ were significant over all lands and were generally stronger than the former. However, the correlation coefficients were still low. One reason might be the nonlinear effects of synoptic systems and the even shorter timescale variability of the diurnal cycle, which may not be reasonably represented in this study because data at a finer resolution were unavailable. Our linear decomposition method also limited the nonlinear effects.

The influence of MJO in the annual cycle of extreme rainfall was second in important and due to the seasonal dependence of MJO activity. The link between MJO and extreme rainfall at the interannual timescale was less important, which means that the linear component of MJO interannual variation did not have essential relations with extreme precipitation.

When the MJO was active over the Maritime Continent, the associated convection brought frequent heavy precipitation. Conversely, when the MJO was inactive, it suppressed the convection activity and associated rainfall and therefore decreased the extremes. The consistent variations in the vertical movement of air at 500 hPa and the OLR field are described in the following paragraphs.

Fig. 6 shows the composited extreme events as a function of eight MJO phases and two ENSO phases. Over northern IC, the extreme total det (Fig. 6a) and extreme frequency def (Fig. 6a1) showed similar changing tendencies along the phase variation of ENSO and MJO. Over the other seven lands, the extreme frequency (figures not shown) also coherently varied with the extreme total. Fig. 6b2 illustrates the effects of convection on extremes with the -OLR over southern IC. When the -OLR anomaly was roughly large and increased from MJO–1 to MJO–3 during El Nino conditions, the corresponding extreme total was also generally large and increased from MJO–1 to MJO–2, but it slightly decreased from MJO–2 to MJO–3. The different tendency from MJO–2 to MJO–3 might have been due to the fact that the OLR was only a necessary but insufficient condition for extreme rainfall. When the -OLR anomaly decreased from MJO–3 to MJO–5 during El Nino conditions (Fig. 6b2), the extreme rainfall was correspondingly reduced (Fig. 6b). During other MJO phases in El Nino conditions, both the -OLR anomaly and extreme total maintained relatively low values. During La Nina conditions, the -OLR anomaly and extreme total varied with the same tendency. A similar coherent variation between the -OLR anomaly and extreme total was also found over the other seven lands (figures not show). Fig. 6c3 illustrates the influence of vertical velocity ω of air at 500 hPa (from NCEP reanalysis II) on extreme precipitation over Sumatra. In El Nino conditions, when the $-\omega$ anomaly reached its peak at MJO–3, the extreme precipitation also reached the maxima (Fig. 6c3). They both fell to minimal values at MJO–5. In La Nina conditions, the peaks shifted to MJO–4 and the minimals shifted to MJO–6. This phase locking change was also found over the other seven lands. Fig. 6b2, c3 reveal that the variation of extreme precipitation could be explained by the anomalous change of convection dynamics.

Generally, El Nino conditions produced more extreme precipitation during MJO–1 to MJO–3 over southern IC, Sumatra, Java, Borneo, and New Guinea, while La Nina conditions mostly produced more extreme precipitation over those lands during MJO–4 to MJO–6. Finally, El Nino conditions largely gained the superiority again during MJO–7 and MJO–8. Over northern IC, LV, and Mindanao, El Nino preferentially affected large extreme precipitation in MJO–5 and MJO–6 (Fig. 6a, g, h), while the behavior of La Nina conditions was very different. During MJO–4 to MJO–5, La Nina generated weak extremes over northern IC, while it produced heavy extremes over

Mindanao. Over LV and Mindanao, La Nina produced more extremes than El Nino did in MJO–4. During MJO–6 to MJO–8, El Nino and La Nina produced similar extreme totals over LV and Mindanao. The dynamical analysis of MJO dependence in regard to the impact of ENSO on extreme precipitation is presented in the following paragraph.

During the first two MJO phases (MJO–1 and MJO–2), the La Nina event was more favorable to moderately higher extreme totals and frequencies than El Nino conditions were (Fig. 6a). This can be clearly seen in Fig. 7, which presents the anomalous evolution of the -OLR and horizontal winds at 850 hPa as a function of MJO and ENSO conditional on extreme events over northern IC. During MJO–1 and MJO–2, the anomalies of low level convergence and latent heating were stronger during La Nina conditions than those during El Nino conditions over northern IC. In this period, the MJO associated anomalous convection was found over the Indian Ocean and northern IC, and it gradually increased in strength and widened its spatial range. However, during El Nino conditions, an anomalous subsidence of Walker circulation caused low level divergence over the Maritime Continent and the surrounding ocean. This subsidence anomaly offset part of the low level convergence anomaly produced by the active phase of MJO over northern IC, which tended to weaken the capacity for extreme event generation. Conversely during La Nina conditions, an anomalous ascent of Walker circulation over the Maritime Continent (not colored in Fig. 7) enhanced the convection over northern IC, even though its strength was weaker than the subsidence anomaly during El Nino conditions. The enhanced convection activity preferentially generated extreme precipitation over northern IC. The contrasting effects on convection of La Nina and El Nino resulted in the moderately higher extremes during La Nina conditions (Fig. 6a). At the same time, an obvious low level divergence anomaly was observed over LV and Mindanao in both ENSO phases, which tended to generate weak extreme rainfall activities in those areas (Fig. 6g, h).

Recall that the evolution of the large–scale circulation related to ENSO and MJO corresponding to the extremes, as shown in Fig. 7, only took place in northern IC. This could partly explain the distinct low or high extreme events over the other seven lands, but not all, because Fig. 7 was only conditional on the extremes over

northern IC. The extremes over the other lands differed in timing from that over northern IC, so phase differences in ENSO and MJO over each land must be one important reason.

In MJO–3 and MJO–4, the MJO associated convection anomaly moved farther east and became stronger over northern IC. During El Nino events, the subsidence over the Maritime Continent offset convection strength over northern IC in both MJO phases. However, the remaining convection anomaly suddenly increased from MJO–3 to MJO–4 because the sample size jumped from 5 to 20 days, which meant that the accumulated convective anomalies strengthened rapidly and therefore increased the extreme rainfall from MJO–3 to MJO–4 in Fig. 6a. The sample size was proportional to the accumulated anomalous convective energy that quantified the heavy precipitation det and its frequency def. The sample size in conjunction with the convergence and divergence pattern determined the change of extreme precipitation in Fig. 6a. In contrast to El Nino conditions, the sample size decreased from 18 to 5 days during La Nina conditions, which decreased the accumulated anomalous convection and so reduced the extremes in Fig. 6a, even though the MJO convection in both MJO phases was equally enhanced by the ascent anomaly of Walker circulation in the Maritime Continent. Meanwhile, suppressed convection anomalies over LV and Mindanao were formed, which were associated with the low amount of extreme precipitation in MJO–3 shown in Fig. 6g, h.

In contrast to previous MJO phases, the sample size remarkably increased to a maximum of 65 days in MJO–5 and to a maximum of 49 days in MJO–6 during El Nino conditions. Nevertheless, the MJO–5 was the most active phase over northern IC, and it was associated with the strongest convective anomaly there among all the MJO phases. This anomalous ascent was generally stronger than the subsidence anomaly produced by El Nino over northern IC, which accumulated huge convective energy during the 65 days and therefore was associated with the maximum amount of extreme precipitation in Fig. 6a. This anomalous convective band extended southeastward until the eastern Tropical Pacific and was enhanced by the anomalous ascent of Walker circulation in the central Tropical Pacific. In MJO–6 and El Nino conditions, this anomalous convective region moved farther east and slightly reduced its accumulated strength, which is reflected in Fig. 6a by the slightly decreased extreme

rainfall total. This anomalous convective band crossed the Philippines and possibly enhanced extreme precipitation over LV (Fig. 6g, h). Meanwhile, the overlap of the subsidence anomalies from MJO and El Nino produced a huge strong downdraft band over the tropical Indian Ocean and the deep tropics of the Maritime Continent. The strong subsidence region in both MJO–5 and MJO–6 may have suppressed the extreme rainfall over southern IC, Sumatra, Java, Borneo, and New Guinea, regardless of slight differences in the MJO phase caused by individual land locations, which can be seen in Fig. 6b–f. During La Nina conditions, the sample size was just a few days. Even though the overlapped convection was observed over northern IC, the accumulated convective activity remained very weak and therefore the extreme precipitation was low (Fig. 6a).

For MJO–7 during El Nino conditions, the MJO associated wet and dry anomalies moved farther east. However, the sample size was dramatically decreased to 12 days, thus the accumulated anomalous convective strength over northern IC was decreased and the associated extreme rainfall was reduced in Fig. 6a. Under the MJO–8 for El Nino conditions, the sample size was only 4 days and a subsidence occurred over part of northern IC. Thus, the extreme precipitation decreased to the minimal amount. During La Nina conditions in MJO–7 and MJO–8, the small sample size caused by the accumulated convective anomalies remained very weak and therefore the extreme precipitation was low (Fig. 6a).

In regard to extremes over the other seven lands, this type of evolution in large–scale circulation anomalies could be explained by a similar dynamic concept (figures not shown), except that the location of convergence and latent heating showed phase shifting despite the different strengths. When the low level northwest–southeast tilted convergence anomaly of MJO traveled eastward across the Maritime Continent accompanied by its divergence counterpart, it encountered the subsidence (ascent) anomaly over the Maritime Continent induced by the El Nino (La Nina) episode. The overlapped updraft (downdraft) anomaly would have enhanced (weaken) the local convection and therefore produced heavy (trivial) extreme precipitation; the combined effects of the opposite anomalies would have likely generated moderate extreme precipitation. Fig. 8 illustrates those processes. Thus, the impact of ENSO on extreme precipitation over the Maritime Continent depended on the MJO phases.

The coherent variation of the extremes in Fig. 6 and the anomalous large-scale circulation in Fig. 7 demonstrated that the dynamical mechanism dominated the extreme precipitation over the tropical warm pool instead of the thermodynamic mechanism, which was consistent with the results of Emori and Brown (2005), Li et al. (2011), and Chou et al. (2012).

We quantified the correlation between extreme precipitation and ENSO as well as the MJO during the local rainy season over Maritime Continent lands from 1980-2013 and found that the impact of ENSO on extremes was dependent on the MJO phases. ENSO tended to impact the extremes by changing its interannual variation component, while MJO influenced the extremes through both the annual cycle and the intraseasonal component of the extreme itself.

Notably, our linear decomposition of extreme precipitation has limitations. For example, it may have missed the nonlinear interactions among the interannual time scale variabilities and the variabilities at shorter timescales. However, this new approach was found to be useful for detecting the impact of the large-scale circulation mode on extreme rainfall over the Maritime Continent region.

5.2 Hindcast experiment

Because of the complexity of land-sea contrasts, with several big islands higher than 2000 m in the region, global models do not always resolve the important topographic features that determine the spatial variability of rainfall at regional scales. The local error in the global model over the Maritime Continent leads to systematic global uncertainties in medium-range weather predictions and climate simulations through planetary wave propagation (Peatman et al., 2013). However, a high-resolution model can capture the local features that arise from uplift condensation due to the topography (Qian and Zubair, 2010), and this improves the predictive performance of the amplitude of the diurnal cycle and mean rainfall (Wu and Hsu, 2009; Love et al., 2011; Dirmeyer et al., 2012) and even the ratio of stratiform to convective precipitation (Boyle and Klein, 2010).

Thus, the CORDEX-SEA project was established with the intent of improving

the coordination of international efforts in RCD research. The hindcast downscaling experiments for current climate were forced by the reanalysis data of ERA–Interim.

The climatological annual cycle in the hindcast experiment (Fig. 9) generally showed reasonable results compared with the results from observations (Fig. 4). Over northern IC, the hindcast experiment successfully simulated the seasonal progression of the boreal summer monsoon climate. The timing of rainy season onset (May), maturing (June–August), withdrawal (September and October), and driest conditions (December–March) were reasonably replicated. However, the regional model produced more precipitation in the rainy season and therefore overestimated the extreme precipitation. The overestimation of rainfall over northern IC was mainly caused by the positive bias in the moisture flux convergence over the Bay of Bengal in the ERA–Interim dataset (Yang et al., 2012), but the maximum extreme frequency in August was properly represented. Over southern IC, the semiannual cycle of rainfall was fairly reproduced compared with the observations. Moreover, the magnitude of rainfall and extreme frequency were reasonable. However, the maximal rainy period took place one month earlier than that for the observed data, and associated peak flattening lowered the maxima of extreme totals. Over Sumatra, the semiannual variation of rainfall was simulated very well except that the magnitude was overestimated compared with the observations. The quantity for the extreme frequency was reasonable, but extreme totals were over produced, which might have been due to the higher extreme intensity in the regional model caused by the effects of the finer grid cumulus convection scheme. The first peak of extreme rainfall was delayed by one month and the second peak was earlier by one month. However, the rainy season was well defined like in the observed case. The clear variation in the rainfall annual cycle over Java was reasonably reproduced with higher amounts relative to the observations, which caused the overestimation of extreme rainfall. Nevertheless, the extreme peak was widened; although the magnitude of extreme frequency was proper. Over Borneo, the semiannual cycle of rainfall was clearly and suitably generated by the model. The extreme wet peak and dry peak were both shifted earlier by one month. The second peaks of the extreme rainfall and associated frequency were higher than those in the observations. The magnitude of extreme frequency was good. Over New Guinea, the seasonal progression of rainfall itself was reasonable, but higher quantities were

obtained in model simulations. Both of the very heavy extreme and frequency peaks had shortened durations and this therefore increased the peaks in the model results. However, the rainy season of extreme rainfall was meaningful. Over LV, the rainfall annual cycle was well simulated. However, the peaks of extreme rainfall and corresponding frequency took place in June as opposed to July in the observations. The magnitude of frequency was reasonable. However, extreme peaks were over generated in the model. Over Mindanao, the hindcast experiment overestimated rainfall in the boreal summer. There appeared to be a monsoon climate shift in Mindanao in the hindcast experiment. However, our focus here was on finding the rainy season, and the pronounced rainfall during June and January relative to the other months in the hindcast experiment was consistent with the observations.

Table 3 gives the correlations between various extreme components of the hindcast experiment and -ONI. The averaged correlation throughout the eight lands for the extreme total of the interannual component and -ONI was 0.32, which was the highest value among all the averaged correlations. Five out of eight correlations between -ONI and the extreme totals of the interannual component passed the 90% significant test. The five lands where this occurred were southern IC, Sumatra, Borneo, New Guinea, and Mindanao. Except over Mindanao, the regional model overestimated the correlations over the other four lands. Other extreme rainfall components of $metAC$, $metIS$, and $metSY$ almost did not relate to ENSO. The averaged correlation between the entire extreme rainfall met and -ONI was very low.

Similar to the observed study, the downscaling results supported the tendency whereby the impact of ENSO on extreme rainfall totals over Maritime Continent lands was mainly through its influence on the interannual component of extreme rainfall. The impact of ENSO was very weak if all the components of extreme rainfall were considered as a whole.

The links between the LMJOI and various extreme components simulated by the hindcast experiment are shown in Table 4. Four out of eight lands showed significant correlations between the LMJOI and the weekly total of extreme rainfall wet. The averaged correlation over all lands was 0.10, which was mainly driven by the averaged correlations from $wetIS$ and $wetAC$ relative to the LMJOI. Significant correlations between $wetIS$ and the LMJOI occurred in more than half of the eight

lands. $wetAC$ showed significant correlations relative to the LMJOI only over four lands. Even though the averaged correlation of the LMJOI relative to $wetSY$ was higher than that relative to $wetAC$, the number of lands with significant correlations in the case of $wetSY$ were less than those in the case of $wetAC$. Therefore, $wetIS$ and $wetAC$ were the main components of the weekly extreme totals wet that were impacted by the MJO. The averaged correlation of $wetIA$ relative to the LMJOI was very small, thus suggesting that there was no relationship between the linear interannual variation component of the extreme precipitation and the MJO.

As a function of ENSO and MJO, the composited accumulated extreme precipitation det is shown in Fig. 10. Over northern IC, the regional model reasonably simulated the variation of extreme precipitation as a function of the ENSO and MJO phases compared with the observations (Fig. 6), except that the quantity was overestimated. Over southern IC, the variation of extreme precipitation was generally reproduced well compared with the observed study data, except the magnitude was underestimated. The proper quantity of extremes under El Nino relative to that under La Nina conditions demonstrated that the impact of the MJO in conjunction with ENSO on extremes was correctly simulated. Over Sumatra under El Nino conditions, the regional model reasonably simulated the increasing tendency from MJO–1 to MJO–3 and the decreasing tendency from MJO–3 to MJO–5. However, the convection was relatively weaker in MJO–7 among all the MJO phases compared with the observations. Under La Nina conditions, the convection strength was overestimated during MJO–5 to MJO–8, which caused the unreasonable variations in the extreme rainfall. Over Java, the general variation of extreme precipitation along the MJO phases was acceptable in La Nina episodes. However, the extreme rainfall in MJO–8 during El Nino episodes was overestimated too much, which induced the unreasonable extreme variations. Over Borneo, the variations of extreme rainfall along the MJO phases were comparable with the observed study in both ENSO phases. Over New Guinea, the variation of extreme rainfall was reasonable except that the extreme magnitude was overestimated during El Nino conditions. Over LV, the extreme rainfall was obviously overestimated during MJO–6 to MJO–8 in El Nino conditions while it was underestimated during MJO–1 to MJO–5 in La Nina conditions. Over Mindanao, the extreme variation was reasonable except that the magnitude was too high relative to the observations. During La Nina, there was only small

variation along the MJO phases, which was unrealistic compared with the observed study.

Generally, the regional model was capable of simulating the extreme variations that occurred along with the changes in the MJO and ENSO. However, in many cases, the magnitudes of extremes were over simulated, which might have been due to the overestimation of the rainfall itself in the regional model. Extreme precipitation involves higher–order statistics and therefore the skill in numerical models was commonly poor relative to that of mean precipitation.

Second, we analyzed the generalized extreme value (GEV) probability density function (PDF) of extreme rainfall over each of the eight lands. Fig. 11 shows the PDFs fitted by a generalized Pareto distribution (Pickands, 1975) to the series of extreme daily precipitation totals det for the analysis period. The robust means and robust variations that were calculated are shown in the figure.

In northern IC, the regional model in the hindcast experiment overestimated both the mean and spread of extreme precipitation. The model underestimated the mean and spread over southern IC, while the PDF location was very close to that in the observations. The hindcast experiment overestimated both the mean and spread of the extremes over Sumatra and Java. Over Borneo, the model only slightly overestimated the mean and spread. While for New Guinea, the regional model overestimated the mean but underestimated the spread of extremes. Over LV, the model moderately overestimated the mean but reduced the spread, and the PDF location was close to the observed location. Over Mindanao, positive biases were produced in the mean and spread of the extremes.

Generally, the regional model reasonably reproduced the phases of the annual climate cycle of rainfall and extremes, but with bias in the amplitude. Qualitatively, the impacts of ENSO and MJO on the extremes were also correctly reproduced in the model. However, the impacts were weaker compared with those in the observed study. As a function of ENSO and MJO phases, the variations of extremes were comparable with those in the observations in most cases. However, the magnitude and spread of extremes were usually overestimated.

5.3 Historical experiment

To conduct a climate change study for future scenarios with CORDEX-SEA project, a historical experiment (control experiment) must be carried out that is forced by a global coupled model. Here, the global model was the HadGEM2-AO, the same model used to force the future projection downscaling. The performance of the HadGEM2-AO was studied by Baek et al. (2013).

First, we checked the annual climate cycle of rainfall, extreme total det, and extreme frequency def in the historical experiment (Fig. 12). The climatological annual cycles in the historical experiment (Fig. 12) were generally reasonable compared with those in the observations (Fig. 4). Over northern IC, the historical experiment reasonably simulated the annual cycle of the boreal summer monsoon climate. The monsoon onset, maturing, withdrawal, and driest season were reasonably reproduced. However, the regional model produced more precipitation in June and July and therefore overestimated the extreme precipitation, but the extreme frequency was quantitatively realistic. Over southern IC, the model produced a semiannual cycle of rainfall of which the phase was twisted somehow by overestimating the rainfall in September. Therefore, the extreme totals in September and October were over generated. The magnitude of the extreme frequency was reasonable. Over Sumatra, the regional model unrealistically produced equal semiannual variation of rainfall that was almost doubled the magnitude compared with that in the observations, which thus induced extreme rainfall totals that were too high. The unequal magnitude semiannual cycles for the extreme total and frequency were realistic. However, the peaks for the extreme total and frequency were delayed by one month. Over Java, the quantity of rainfall was almost doubled and the phase of the annual cycle was delayed by one or two months relative to that in the observations. The magnitude of the extreme total was overestimated, but the frequency number was reasonable. The overestimation of rainfall in December and May resulted in two peaks in the extreme total, which covered the real peak in January in observations. Over Borneo, the variation of the annual cycle was similar to the observed cycle except that the rainfall magnitude was overestimated. The magnitude of the frequency was reasonable, but the extreme total was overestimated.

The weak peaks in the extreme frequency and total corresponding to the semiannual annual cycle of rainfall were unrealistic. Over New Guinea, all variables in the rainy season were overestimated in the historical experiment. The annual cycles were consistently clear in all the variables, but the peaks occurred one month earlier than the observed ones. Over LV, the annual cycle was clear but the sudden arrival of the rainy season in May was unrealistic compared with the gradual increase of rainfall in May and June in the observations. Rainfall and extreme totals were overestimated in the rainy season. Over Mindanao, the clear annual cycle generated by the model was unrealistic compared with the observed cycle, which was evenly distributed in all months. Rainfall and corresponding extremes in the rainy season were overestimated, but the magnitude of the extreme frequency was comparable with that in the observations. The regional model generated a peak of extreme precipitation in June–September, while the observation peak took place in January.

Second, we tried to find the links between extreme precipitation in our historical experiment and the observed ENSO or MJO data. However, the results were unsatisfactory (data not shown). Although many studies have shown that precipitation simulated in historical experiments with a global climate model (GCM) (e.g. Tebaldi et al., 2006) or RCM (e.g. Meehl and Tebaldi, 2004; Sillmann and Roekner, 2008; Alexander and Arblaster, 2009) is reasonable, simulating large–scale circulation modes such as ENSO and MJO made it difficult to achieve the same level of skills in the historical experiments. On representing ENSO, the HadGEM2–AO missed most extreme ENSO events such as in 1983, 1989, and 1998 (figure not shown). Nevertheless, the principal component (PC)1 and PC2 of the MJO index in the HadGEM2–AO barely showed correlations with the PCs of observations (figure not shown). In fact, Leloup et al. (2007) showed that none of the GCMs in the Intergovernmental Panel on Climate Change (IPCC) Fourth Assessment Report database were sufficiently good at capturing all aspects of the extent, location, and timing of ENSO events. This therefore seems to be a common shortcoming in CORDEX historical downscaling experiments given their dependence on SST anomalies of coupled GCMs.

Even though the interannual and intraseasonal variation of extreme precipitation in our historical experiment was unsatisfactory, we were able to investigate other aspects of the extremes such as the mean and spread. Fig. 11 compares the PDFs

of extremes between the observations and the historical experiment. Over northern IC, the regional model in the historical experiment overestimated both the mean and spread of extreme precipitation. While the model reduced the mean and spread of extremes over southern IC, the location of the model PDF was very close to that of the observations. In general, the skills were better than the skills in the hindcast experiment. The model overestimated both the mean and spread over other lands. In most cases, the biases were larger than those in the hindcast experiment.

In future studies, a multi-model ensemble of all the CORDEX-SEA data needs to be considered to find the reliable and robust extreme precipitation events in the historical downscaling experiments.

5.4 Future projections

The sophisticated circulation and thermodynamic forcing over the Maritime Continent create many difficulties for hydrological and agriculture management. In particular, high-resolution information is necessary for developing warning systems, and this can be derived from fine-grid experiments that not only reflect the important topographic effects, but also project consistent signs of climate change (Smith et al., 2013). Thus, extreme precipitation downscaling with a regional model is an important approach to study fine-scale climate changes in projected scenarios (e.g., Christensen and Christensen, 2004; Fowler et al., 2007; Im and Kwon, 2007; Im et al., 2007)

Projected extreme precipitation changes imply possible changes in floods. several studies have mentioned that heavy precipitation will likely increase in the 21st century over many areas of the globe (Fowler and Hennessy, 1995), such as over the West Pacific (e.g. Cai et al., 2012), Africa (e.g. Shongwe et al., 2009, 2011), Korea (Im et al., 2007), and tropical regions (IPCC 2012). However, extreme precipitation change research over SEA has been studied less intensively than that over other regions.

To analyze changes in extremes in future projections with Down-45 and Down-85 in our study, we selected two cases to evaluate the differences from the historical experiment. Specifically, the near future of Down-45 and far future of Down-85

were chosen to investigate the impact of greenhouse gas emissions as the situation worsens over time.

The changes in extreme rainfall could be detected by the probability distribution (Fig. 13). The shifting of generalized Pareto distributions for the Down–45 and Down–85 experiments relative to that in the historical experiments explained or inferred the changes in the frequency, mean, and variation of extreme precipitation. Over northern IC, the Down–45 produced slightly less extreme precipitation, while the Down–85 produced slightly more extreme rainfall. The daily variability of extremes in both experiments were increased. In contrast to northern IC, both future projections showed slightly decreased extreme precipitation in the future over southern IC. However, the variability changed in the opposite direction. The location of the PDF in the Down–45 was almost the same as that in the historical experiment, which means that the quantity of the most frequent extremes did not change. Over Sumatra, the extreme rainfall was moderately decreased, but no monotonic tendency in variation was found. For Java, the model showed slightly increased and then decreased extreme rainfall. The variability changed in the same way. It was hard to distinguish the differences in the PDFs of the three experiments over Borneo. Both the mean and variation were continually and slightly increased in the future. The future projection over New Guinea showed moderately reduced extremes with a general increasing trend for the variabilities. Over LV, the mean increased slightly and the variation increased by quite a large amount in the future. Mindanao showed increasing trends for both the mean and variation of the extremes in the future. Generally, there was no clear trend in the mean of extremes in our future projections over the Maritime Continent. However, the daily variability of extremes showed increasing trends over most land areas.

In fact, Manton et al. (2001) studied the extreme rainfall during the past few decades over SEA and they found that there was no clear trend of extreme precipitation over Indonesia, Malaysia, Myanmar, the Philippines, and Vietnam, except that Thailand showed a significant increasing signal in the proportion of total rainfall from extremes. Over the Indo–Pacific region as a whole, the precipitation trends are mixed (Caesar et al., 2011). In contrast, the global results of Alexander et al. (2006) showed consistent trends towards wetter conditions.

In this study, we assessed possible changes in the near future (RCP 4.5; 2021–2045) and far future (RCP 8.5; 2071–2095) extreme precipitation amounts through return period analysis over the Maritime Continent. A return period approach has been used in several studies of extreme precipitation (Fowler and Hennessy, 1995; Hennessy et al., 1997). The return value for a return period of T days is defined as the precipitation amount that is exceeded by a daily extreme with a probability of 1/T. A return period is the average interval between events of the same magnitude. In this study, we analyzed return values of daily extreme precipitation amounts with recurrences within 100 days. So, the threshold for a return period of 100 days is the precipitation amount that would be expected once every 100 days. Return values for return periods in excess of 100 days were considered less reliable because the samples for very extreme daily rainfall corresponding to longer return periods was few and thus the results were not presented here. In our study, the return period for extreme precipitation was considered only during rainy season, and we might understand this by imagining that all of the rainy season was concatenated.

Fig. 14 provides the return value versus return period comparisons between the future projections and our historical experiment. Over norther IC, we wanted to look at the large return values that could critically impact society, for example, ones with return values higher than 20 mm/day. The return period became shorter in the Down–45 and even shorter in the Down–85. For extreme events amounting to 30 mm/day, the return period was around 25 days in the years simulated by the historical experiment, while it was shortened to 15 days in the Down–45 and about 9 days in the Down–85 projections. Similar to northern IC, the return period became shorter in the future over southern IC. For instance, extreme events amount to 60 mm/day had a return beyond 100 days, however, such events happened around every 65 days in the Down–45 and 45 days in the Down–85 experiments. The case in Sumatra was complicated in that an extreme event of the same quantity returned in a shorter time interval in the Down–45 than in the Down–85 where the return period was longer. Over Java, a heavy extreme event appeared to return in a shorter period in the future. However, the return period was shorter in the Down–45 than in the Down–85. Over Borneo, the situation was similar to northern IC and southern IC but different in that for the same return period, the corresponding return values were very close for the Down–45 and Down–85 projections. Over New Guinea, the

return values as a function of the return period almost overlapped, especially for the historical experiment and the Down–45, which means that the same amount of extreme precipitation returned over similar period of time in the present and in the future. Over LV, the Down–45 and Down–85 did not show many differences; they both had lengthened return periods for the same amount of extreme rainfall. Over Mindanao, the situation for the heavy extreme events was similar to that over Sumatra. An extreme event of the same amount tried to return in shorter times in the Down–45 and in longer times in the Down–85 in the future compared to present years.

Note that the dynamical mechanism dominated the extreme precipitation over the tropical warm pool instead of the thermodynamic mechanism. The lengthened return period might be due to a circulation change, which could reduce the water vapor supply in the convergence band or shift the convergence band over the Maritime Continent.

6. Discussion and conclusion

In this study, we analyzed extreme precipitation in the rainy season over the Maritime Continent from observations, dynamic downscaling of a hindcast experiment forced by the ERA–Interim reanalysis dataset, a historical experiment forced by the HadGEM2–AO global coupled model, as well as downscaling for near future RCP4.5 and far future RCP8.5 projections forced by the HadGEM2–AO output.

We quantified the correlations between observed extreme precipitation and ENSO as well as MJO during the local rainy season over Maritime Continent lands from 1980–2013 and found that the impact of ENSO on the extremes was dependent on the MJO phases. ENSO tended to impact the extremes by changing its interannual variation component, while MJO influenced the extremes through both the annual cycle and intraseasonal component of the extreme itself.

When the low–level northwest–southeast tilted convergence anomaly of MJO traveled eastward across the Maritime Continent accompanied by its divergence counterpart, it encountered the subsidence (ascent) anomaly over the Maritime Continent during El Nino (La Nina) episodes. The overlapped updraft (downdraft) anomaly enhanced (weaken) the local convection and therefore produced heavy (trivial) extreme precipitation. The compensation of opposite anomalies tended to generate moderate extreme precipitation. Fig. 8 illustrated those processes.

Generally in the hindcast experiment, the regional model reasonably reproduced the phases of the annual climate cycle for rainfall and extremes, but with biases in the amplitude. Qualitatively, the impacts of ENSO and MJO on the extremes were also correctly repeated in the model. However, the impacts were weaker compared with those in the observed study. As a function of the ENSO and MJO phases, the variations of extremes were comparable with that in the observations for most cases. However, the magnitude and spread of extremes were usually overestimated, which might have been due to the overestimation of rainfall itself in the regional model.

The climatological annual cycles in the historical experiment were generally reasonable compared with those in the observations. However, the links between the extreme precipitation and ENSO or MJO were unsatisfactory, which was caused

by the unrealistic representation of ENSO and MJO in the large-scale forcing of HadGEM2-AO compared to the observed ENSO and MJO. In future studies, the links between model extremes and model ENSO or MJO need to be investigated to show the model dynamics on extremes that were impacted by the large circulation mode. In most cases, biases in the extreme precipitation were larger than those in the hindcast experiment. The historical experiment was forced by the HadGEM2 model whose low-level circulation generally showed negative bias in terms of the height and positive convergence bias for most times over the Maritime Continent (Yang, 2014). Those circulation biases might have caused excessive rainfall in the downscaling result.

In the downscaling experiments for future projections, there was no clear trend of change in the mean of extremes. However, the daily variability of extremes showed increasing trends over most lands. Over northern IC, southern IC, Borneo, and Java, large extreme rainfall will likely become more frequent in the future. The extremes over LV tended to show the opposite situation. No large changes are forecasted over New Guinea. The extremes over Sumatra and Mindanao showed uncertain changes in the future.

Our study does have limitations. Linear decomposition of rainfall conditional on extreme precipitation may have missed the nonlinear interactions of slow variation at the interannual time scale with other quick variabilities. However, this new approach was efficient for detecting the impact of various large-scale circulation modes on the extreme rainfall over the Maritime Continent region.

A multi-model ensemble of all the CORDEX-SEA project data needs to be considered in future studies to provide further reliable and robust estimates of extreme precipitation and its links to large-scale precursors in the model results.

Acknowledgements

I would like to thank Dr. Moosup Kim for advice on choosing the extreme distribution. I am also grateful for discussions with Prof. Fei-Fei Jin and reviews from Prof. Joong-Bae Ahn and Prof. Myongin Lee who provided insightful and constructive suggestions. The author was supported by the the Asia-Pacific Economic Cooperation (APEC) Climate Center, Korea.

References

AghaKouchak A, Behrangi A, Sorooshian S, Hsu K, Amitai E (2011) Evaluation of satellite-retrieved extreme precipitation rates across the central United States. J Geophys Res 116, doi:10.1029/2010JD014741.

Alexander LV, et al (2006) Global observed changes in daily climate extremes of temperature and precipitation. J Geophys Res Atmos 111:D05109.

Alexander LV, Arblaster JM (2009) Assessing trends in observed and modelled climate extremes over Australia in relation to future projections, Int J Climatol 29:417–435

Alexander LV, Uotila P, Nicholls N (2009) The influence of sea surface temperature variability on global temperature and preciptation extremes. J Geophys Res 114:D18116, doi:10.1029/2009JD012301.

Allan RP, Soden BJ (2008) Atmospheric warming and the amplification of precipitation extremes. Science 321:1481–1484.

Baek HJ and coauthors (2013) Climate change in the 21st century simulated by HadGEM2-AO under representative concentration pathways. Asia Pac J Atmos Sci 49:603–618.

Beljaars ACM (1994) The parameterization of surface fluxes in large-scale models under free convection. Quart J Roy Meteor Soc 121:255–270.

Boyle, J., and S. A. Klein, 2010: Impact of horizontal resolution on climate model forecasts of tropical precipitation and diabatic heating for the TWP-ICE period, J Geophys Res 115:16 DOI: 10.1029/2010JD014262

Caesar J, Alexander LV, Trewin B, Tse-ring K, Sorany L, Vuniyayawa V, Keosavang N, Shimana A, Htay MM, Karmacharya J (2011) Changes in temperature and precipitation extremes over the Indo-Pacific region from 1971 to 2005. Int J Climatol 31:791–801.

Cai W, Lengaigne M, Borlace S, Collins M, Cowan T, McPhaden MJ, Timmermann A, Power S, Brown J, Menkes C (2012) More extreme swings of the South Pacific convergence zone due to greenhouse warming. Nature 488:365–369.

Chang C-P, Liu C, Kuo H (2003) Typhoon Vamei: An equatorial tropical cyclone formation, Geophys Res Lett 30:1150, doi:10.1029/2002GL016365.

Chang C-P, Wang Z, J Ju, Li T (2004) On the relationship between western Maritime Continent monsoon rainfall and ENSO during northern winter. J Clim 17:665–672.

Chang C-P, Wang Z, McBride J, Liu C-H (2005) Annual cycle of Southeast Asia-Maritime

Continent rainfall and the asymmetric monsoon transition. J Clim 18:287–301.

Cheang BK (1977) Synoptic features and structures of some equatorial vortices over the South China Sea in the Malaysian region during the winter monsoon of December 1973. Pure Appl Geophys 115:1303–1333.

Chou C, Chen C, Tan P–H, Chen K–T (2012) Mechanisms for global warming impacts on precipitation frequency and intensity. J Clim 25:3291–3306.

Christensen OB, Christensen JH (2004) Intensification of extreme European summer precipitation in a warmer climate. Global Planet Change 44:107–117

Collins WD, et al. (2004) Description of the NCAR Community Atmosphere Model (CAM 3.0). NCAR Tech. Note NCAR/TN–464+STR. 214 pp.

Davies HC, Turner RE (1977) Updating prediction models by dynamical relaxation: an examination of the technique. Quart J R Meteor Soc 103:225–245.

Dee DP, and coauthors (2011) The EAR–Interim reanalysis: configuration and performance of the data assimilation system. Quart J Roy Meteor Soc 137:553–597.

Dirmeyer PA, et al (2012) Simulating the diurnal cycle of rainfall in global climate models: resolution versus parameterization. Climate Dynamics, 39:399–418.

Dyer AJ, Hicks BB (1970) Flux–gradient relationships in the constant flux layer. Quart J Roy Meteor Soc 96:715–721.

Emori S, Brown S (2005) Dynamic and thermodynamic changes in mean and extreme precipitation under changed climate. Geophys Res Lett 32:L17706.

Fowler AM, Hennessy KJ (1995) Potential impacts of global warming on the frequency and magnitude of heavy precipitation. Nat Hazards 11:283–303.

Fowler HJ, Ekström M, Blenkinsop S, Smith AP (2007) Estimating change in extreme European precipitation using a multimodel ensemble. J Geophys Res 112:D18104, doi:10.1029/2007JD008619.

Hendon HH, Zhang CD, Glick JD (1999) Interannual variation of the Madden–Julian Oscillation during austral summer. J Clim 12:2538–2550.

Hegerl GC, Wallace JM (2002) Influence of patterns of climate variability on the difference between satellite and surface temperature trends. J Clim 15:2412–2428.

Hennessy KJ, Gregory JM, Mitchell JFB (1997) Changes in daily precipitation under enhanced greenhouse conditions. Clim Dyn 13:667–680.

Holland GJ (1986) Interannual variability of the Australian summer monsoon at Darwin: 1952–82. Mon Wea Rev 114:594–604.

Hong S-Y, Dudhia J, Chen SH (2004) A Revised Approach to Ice Microphysical Processes for the Bulk Parameterization of Clouds and Precipitation. Mon Wea Rev 132:103-120.

Hong SY, Noh Y, Dudhia J (2006) A new vertical diffusion package with an explicit treatment of entrainment processes. Mon Wea Rev 134:2318-2341.

Huang et al. (2014) Extended Reconstructed Sea Surface Temperature Version 4 (ERSST.v4). Part I: Upgrades and intercomparisons. J Clim doi:10.1175/JCLI-D-14-00006.1.

Im E-S, Kim M-H, Kwon W-T, Steven C (2007) Projected change in mean and extreme climate over Korea from a double-nested regional climate model simulation. J Meteor Soc Jpn 85:717-732

Im E-S, Kwon W-T (2007) Characteristics of extreme climate sequences over Korea using a regional climate change scenario. SOLA 3:17-20

IPCC (2012) Managing the Risks of Extreme Events and Disasters to Advance Climate Change Adaptation. A Special Report of Working Groups I and II of the Intergovernmental Panel on Climate Change [Field CB, Barros V, Stocker TF, Qin D, Dokken DJ, Ebi KL, Mastrandrea MD, Mach KJ, Plattner G-K, Allen SK, Tignor M, Midgley PM (eds.)]. Cambridge University Press, Cambridge, UK, and New York, NY, USA, 582 pp.

Jones C, Waliser DE, Lau KM, Stern W (2004) Global occurrences of extreme precipitation and the Madden-Julian oscillation: Observations and predictability. J Clim 17:4575-4589.

Joyce RJ, Janowiak JE, Arkin PA, Xie P (2004) CMORPH: A method that produces global precipitation estimates from passive microwave and infrared data at high spatial and temporal resolution. J Hydrometeorol 5:487-503.

Kanamitsu M, Ebisuzaki W, Woollen J, Yang S-K, Hnilo JJ, Fiorino M, Potter GL (2002) NCEP-DOE AMIP-II Reanalysis (R-2). Bull Am Meteor Soc 83:1631-1643.

Kenyon J, Hegerl GC (2010) Influence of modes of climate variability on global precipitation extremes. J Clim 23:6248-6262.

Klemp JB, Wilhelmson R (1978) The simulation of three-dimensional convective storm dynamics. J Atmos Sci 35:1070-1096.

Laprise R (1992) The Euler Equations of Motion with Hydrostatic-Pressure as an Independent Variable. Monthly Weather Review 120:197-208.

Lau KM, Chan PH (1983) Short-term climate variability and atmospheric teleconnections

from satellite–observed outgoing longwave radiation. Part II: Lagged correlations. J Atmos Sci 40:2751–2767.

Leloup J, Lengaigne M, Boulanger JP (2007) Twentieth century ENSO characteristics in the IPCC database, Clim Dyn 30:277–291.

Li F, Collins W, Wehner M, Williamson D, Olson J, Algieri C (2011) Impact of horizontal resolution on simulation of precipitation extremes in an aqua–planet version of Community Atmospheric Model (CAM3). Tellus 63:884–892.

Liebmann B, Smith CA (1996) Description of a complete (interpolated) outgoing longwave radiation dataset. Bull Am Meteor Soc 77:1275–1277.

Love BS, Matthews AJ, Lister G (2011) The diurnal cycle of precipitation over the Maritime Continent in a high–resolution atmospheric model, Q J R Meteorol Soc 137:934–947.

Madden RA, Julian PR (1994) Observations of the 40–50–day tropical oscillation: A review. Mon Wea Rev 122:814–837.

Manton MJ, Della–Marta PM, Haylock MR, Hennessy KJ, Nicholls N, Chambers LE, Collins DA, Daw G, Finet A, Gunawan D (2001) Trends in extreme daily rainfall and temperature in Southeast Asia and the South Pacific: 1961–1998. Int J Climatol 21:269–284.

McBride JL, Nicholls N (1983) Seasonal relationships between Australian rainfall and the Southern Oscillation. Mon Wea Rev 111:1998–2004.

Meehl GA (1987) The annual cycle and interannual variability in the tropical Pacific and Indian Ocean region. Mon Wea Rev 115:27–50.

Meehl GA, Tebaldi C (2004) More intense, more frequent and longer lasting heat waves in the 21st century, Science, 305:994–997.

Ooyama KV (1990) A Thermodynamic Foundation for Modeling the Moist Atmosphere. Journal of the Atmospheric Sciences 47:2580–2593.

Peatman SC, Matthews AJ, Stevens DP (2013) Propagation of the Madden–Julian Oscillation through the Maritime Continent and scale interaction with the diurnal cycle of precipitation. Quarterly Journal of the Royal Meteorological Society. 140:814–825.

Pickands J (1975) Statistical inference using extreme order statistics. Ann Stat 3:119–131.

Qian JH, Zubair L (2010) The effect of grid spacing and domain size on the quality of ensemble regional climate downscaling over South Asia during the northeasterly monsoon. Monthly Weather Review, 138:2780–2802.

Paulson CA (1970) The mathematical representation of wind speed and temperature

profiles in the unstable atmospheric surface layer. J Appl Meteor 9:857–861.

Rasmusson EM, Carpenter TH (1982) Variations in tropical sea surface temperature and surface wind fields associated with the Southern Oscillation/El Nino. Mon Wea Rev 110:354–384.

Rasmusson EM, Wallace JM (1983) Meteorological aspects of the El Nino/Southern Oscillation. Science 222:1195–1202.

Shongwe ME, van Oldenborgh GJ, van den Hurk B, de Boer B, Coelho CAS, van Aalst MK (2009) Projected changes in mean and extreme precipitation in Africa under global warming. Part I: Southern Africa. J Clim 22:3819–3837.

Shongwe ME, van Oldenborgh GJ, van den Hurk B, van Aalst M (2011) Projected changes in mean and extreme precipitation in Africa under global warming. Part II: East Africa. J Clim 24:3718–3733.

Sillmann J, Roekner E (2008) Indices for extreme events in projections of anthropogenic climate change, Clim. Change, 86:83–104.

Skamarock WC, Klemp JB (1992) The Stability of Time-Split Numerical-Methods for the Hydrostatic and the Nonhydrostatic Elastic Equations. Monthly Weather Review 120:2109–2127.

Skamarock WC, Klemp JB, Dudhia J, Gill DO, Barker DM, Wang W, Powers JG (2005) A description of the advanced research WRF version 2. NCAR tech notes-468 + STR

Smith I, Moise A, Katzfey J, et al. (2013) Regional-scale rainfall projections: Simulations for the New Guinea region using the CCAM model. Journal of Geophysical Research: Atmospheres 118:1271–1280.

Solomon S, Qin D, Manning M, Chen Z, Marquis M, Averyt KB, Tignor M, Miller HL (2007) Climate change 2007—the physical science basis: Working group I contribution to the fourth assessment report of the IPCC (Vol. 4). Cambridge University Press, Cambridge, UK, and New York, NY, USA.

Tanaka M (1994) The onset and retreat dates of the austral summer monsoon over Indonesia, Australia and New Guinea. J Meteor Soc Jpn 72:255–267.

Tangang FT, Juneng L, Salimun E, Vinayachandran PN, Seng YK, Reason CJC, Behera SK, Yasunari T (2008) On the roles of the northeast cold surge, the Borneo vortex, the Madden–Julian oscillation, and the Indian Ocean dipole during the extreme 2006/2007 flood in southern Peninsular Malaysia. Geophys Res Lett 35:L14S07, doi: 10.1029/2008GL033429

Tebaldi C, Hayhoe K, Arblaster JM, Meehl GA (2006) Going to the extremes: An

intercomparison of model-simulated historical and future changes in extreme events, Clim. Change 79:185–211.

Tewari M, Chen F, Wang W, Dudhia J, LeMone MA, Mitchell K, Ek M, Gayno G, Wegiel J, Cuenca RH (2004) Implementation and verification of the unified NOAH land surface model in the WRF model. 20th Conference on Weather Analysis and Forecasting/16th Conference on Numerical Weather Prediction, pp. 11–15.

Tiedtke M (1989) A comprehensive mass flux scheme for cumulus parameterization in large-scale models. Mon Wea Rev, 117:1779–1800.

Wang B (2006) The Asian Monsoon. Springer Science & Business Media.

Webb EK (1970) Profile relationships: The log-linear range, and extension to strong stability. Quart J Roy Meteor Soc 96:67–90.

Westra S, Alexander LV, Zwiers FW (2013) Global increasing trends in annual maximum daily precipitation. J Clim 26:3904–3918.

Wheeler MC, Hendon HH (2004) An all-season real-time multivariate MJO index: Development of an index for monitoring and prediction. Mon Wea Rev 132:1917–1932.

Wicker LJ, Skamarock WC (2002) Time-splitting methods for elastic models using forward time schemes. Monthly Weather Review 130:2088–2097.

Wu CH, Hsu HH (2009) Topographic influence on the MJO in the Maritime Continent. Journal of Climate 22:543–5448.

Yang H-W (2013) Revision of climate change by dynamic downscaling over the Maritime Continents. APCC Tech Report.

Yang H-W (2014) Dynamic downscaling of climate change over the Maritime Continents. APCC Tech Report.

Yang H-W, Wang B (2015) Partial lateral forcing experiments reveal how multi-scale processes induce devastating rainfall: A new application of regional modeling. Clim Dyn 45:1157–1167.

Yang H-W, Wang B, Wang B (2012) Reducing biases in regional climate downscaling by applying Bayesian model averaging on large-scale forcing. Clim Dyn 39:2523–2532.

Yatagai A, Kamiguchi K, Arakawa O, Hamada A, Yasutomi N, Kitoh A (2012) APHRODITE: Constructing a long-term daily gridded precipitation dataset for Asia based on a dense network of rain gauges. Bull Am Meteor Soc 93:1401–1415.

Zhang D-L, Anthes RA (1982) A high-resolution model of the planetary boundary layer

sensitivity tests and comparisons with SESAME–79 data. J Appl Meteor 21:1594–1609.

Zhang C–X, Wang Y–Q, Hamilton K (2011) Improved representation of boundary layer clouds over the southeast pacific in ARW–WRF using a modified Tiedtke cumulus parameterization scheme. Mon Wea Rev 139:3489–3513.

Tables

Table 1 Correlation between various component of extremes and the Oceanic Nino Index (ONI) over northern the Indo-China Peninsula (IC), southern IC, Sumatra, Java, Borneo, New Guinea, Luzon and Visayas (LV), and Mindanao. The *metAC*, *metIA*, *metIS*, and *metSY* denote the monthly totals of *rainAC*, *rainIA*, *rainIS*, and *rainSY* conditional on extreme events, respectively. Colored numbers mean that the correlation passed the 90% significant test.

-ONI vs. extreme	metAC	metIA	metIS	metSY
Northern IC	0.02	**0.3**	-0.04	0.09
Southern IC	-0.06	**0.48**	-0.04	0.0
Sumatra	0.1	**0.21**	0.06	**0.13**
Java	-0.06	**0.29**	-0.07	0.0
Borneo	**0.2**	**0.51**	0.05	0.08
New Guinea	0.04	**0.45**	-0.08	0.03
LV	**0.11**	**0.45**	**0.12**	**0.14**
Mindanao	**0.17**	**0.51**	0.01	**0.18**
Average	0.05	0.4	0.0	0.08

Table 2 Correlation between various extreme components and the localized the Madden–Julian Oscillation (MJO) index (LMJOI). The *wetAC*, *wetIA*, *wetIS*, and *wetSY* represent the weekly totals of *rainAC*, *rainIA*, *rainIS*, and *rainSY* conditional on extreme events, respectively. The LMJOI was weekly aggregated before calculating the correlation coefficients. Colored numbers mean that the correlation passed the 90% significant test.

LMJOI vs. extreme	wet	wetAC	wetIA	wetIS	wetSY
Northern IC	**0.19**	**0.18**	**-0.11**	**0.25**	-0.06
Southern IC	**0.15**	**0.12**	0.06	**0.1**	**0.13**
Sumatra	**0.1**	0.07	-0.01	**0.17**	0.02
Java	**0.15**	**0.13**	**-0.1**	**0.16**	**0.08**
Borneo	**0.14**	**0.11**	0.02	**0.14**	**0.1**
New Guinea	**0.08**	**0.09**	-0.02	**0.12**	-0.03
LV	**0.18**	**0.19**	-0.03	**0.23**	0.02
Mindanao	**0.21**	**0.2**	0.03	**0.19**	**0.14**
Average	0.15	0.14	-0.02	0.17	0.05

Table 3 Correlation between various extreme components of the hindcast experiment and -ONI. The *metAC*, *metIA*, *metIS*, and *metSY* denote the monthly totals of *rainAC*, *rainIA*, *rainIS*, and *rainSY* conditional on extreme events of the hindcast experiment, respectively. Colored numbers mean that the correlation passed the 90% significant test.

-ONI vs. extreme	metAC	metIA	metIS	metSY
Northern IC	-0.04	0.09	0.02	0.01
Southern IC	-0.07	**0.55**	0.07	**0.25**
Sumatra	0.1	**0.48**	0.0	**0.17**
Java	**-0.33**	0.07	**-0.31**	-0.1
Borneo	**0.2**	**0.52**	0.0	**0.2**
New Guinea	0.1	**0.52**	0.09	0.08
LV	0.05	0.11	0.04	0.06
Mindanao	**-0.18**	**0.24**	**-0.15**	-0.06
Average	-0.02	0.32	-0.03	0.08

Table 4 Correlation between the LMJOI and various extreme components of the hindcast experiment. The *wetAC*, *wetIA*, *wetIS*, and *wetSY* represent the weekly totals of *rainAC*, *rainIA*, *rainIS*, and *rainSY* conditional on extreme events in the hindcast experiment, respectively. The LMJOI was weekly aggregated before calculating the correlation coefficients. Colored numbers mean that the correlation passed the 90% significant test.

LMJOI vs. extreme	wet	wetAC	wetIA	wetIS	wetSY
Northern IC	**0.17**	**0.14**	0.07	**0.18**	0.04
Southern IC	**0.24**	**0.14**	0.09	**0.23**	0.09
Sumatra	0.06	-0.01	-0.02	**0.13**	**0.12**
Java	**0.11**	0.08	**-0.11**	**0.11**	**0.11**
Borneo	**0.13**	**0.1**	**0.11**	0.07	**0.18**
New Guinea	0.0	0.0	**-0.16**	0.04	-0.02
LV	0.07	**0.09**	0.03	0.05	0.04
Mindanao	0.05	0.01	-0.03	**0.08**	0.05
Average	0.1	0.07	0.0	0.11	0.08

Figures

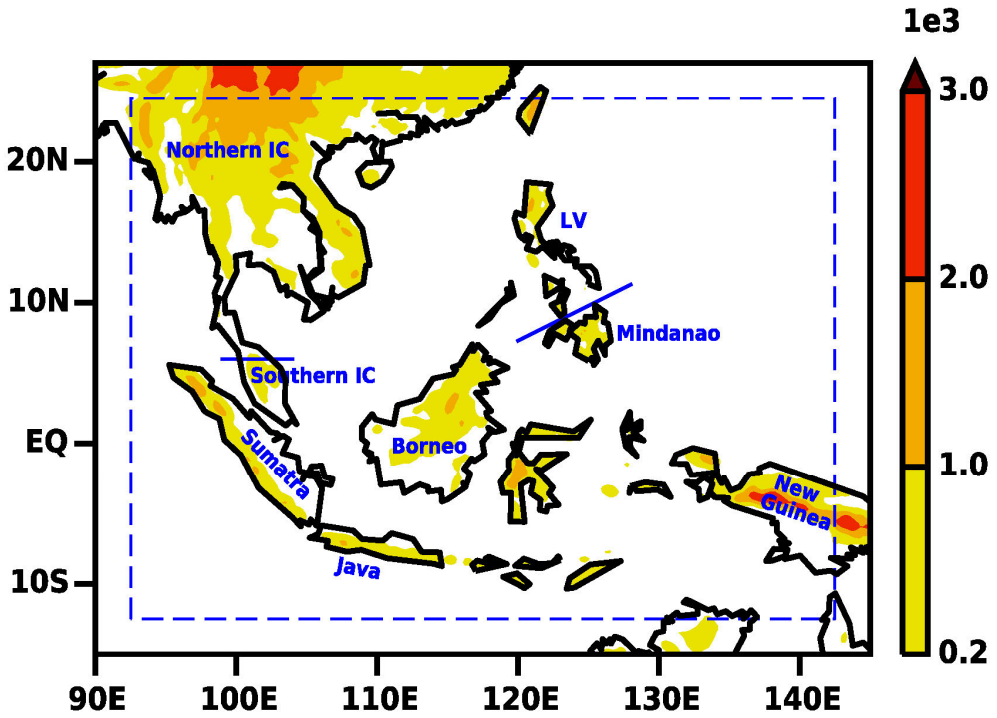

Figure 1 Domain (15°S–27°N, 90–145°E), buffer zone (outside of blue dashed lines: 12.5°S–24.5°N, 87.5–142.5°E), and topography (color shades are in units of meters). Analysis areas over land enclosed by blue lines refer to northern the Indo-China Peninsula (IC), southern IC, Sumatra, Java, Borneo, New Guinea, Luzon and Visayas (LV), and Mindadao.

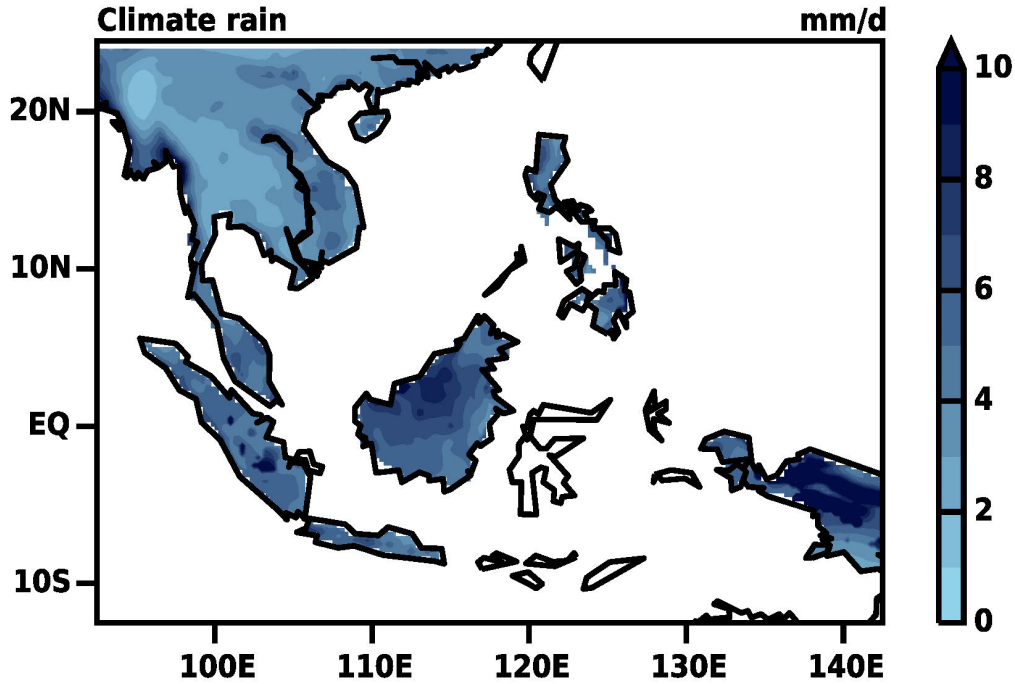

Figure 2 Climatological rainfall of daily data.

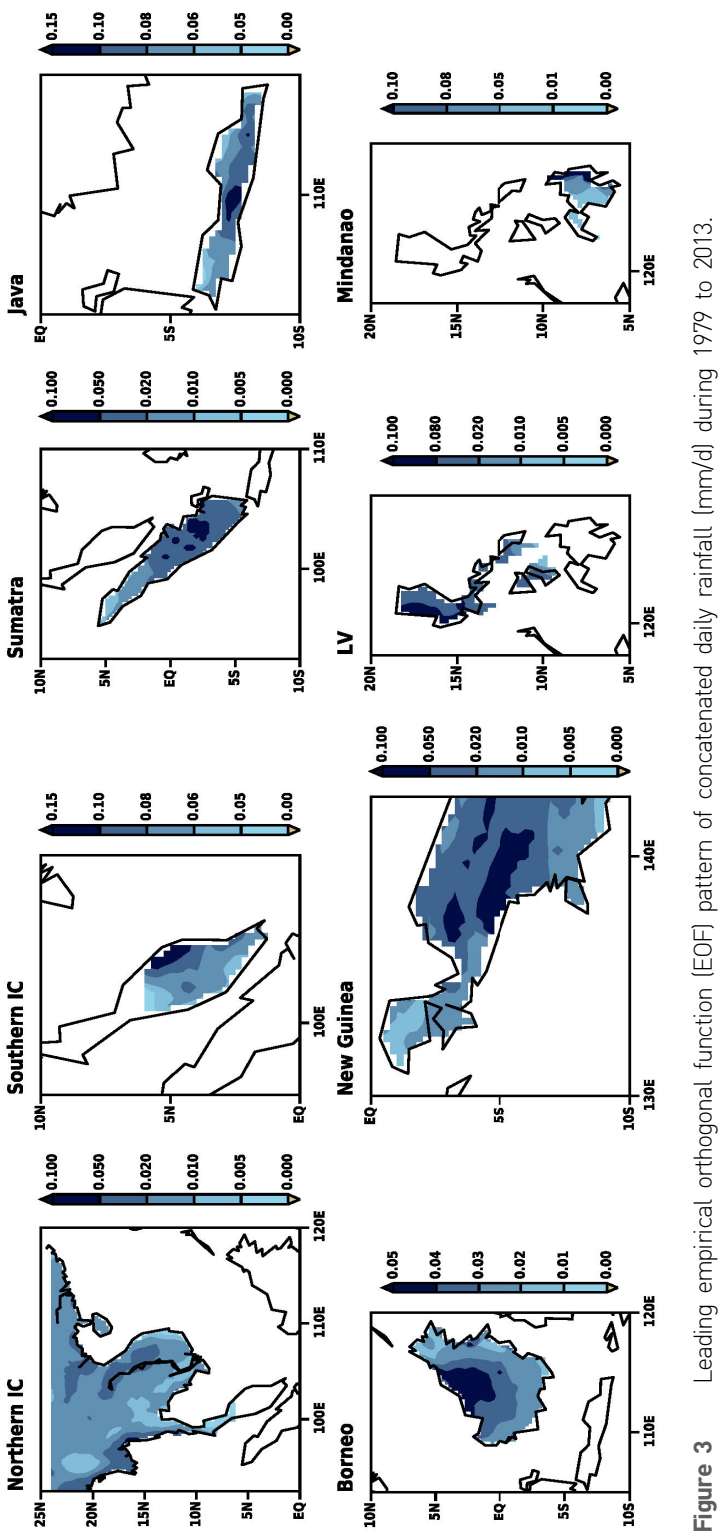

Figure 3 Leading empirical orthogonal function (EOF) pattern of concatenated daily rainfall (mm/d) during 1979 to 2013.

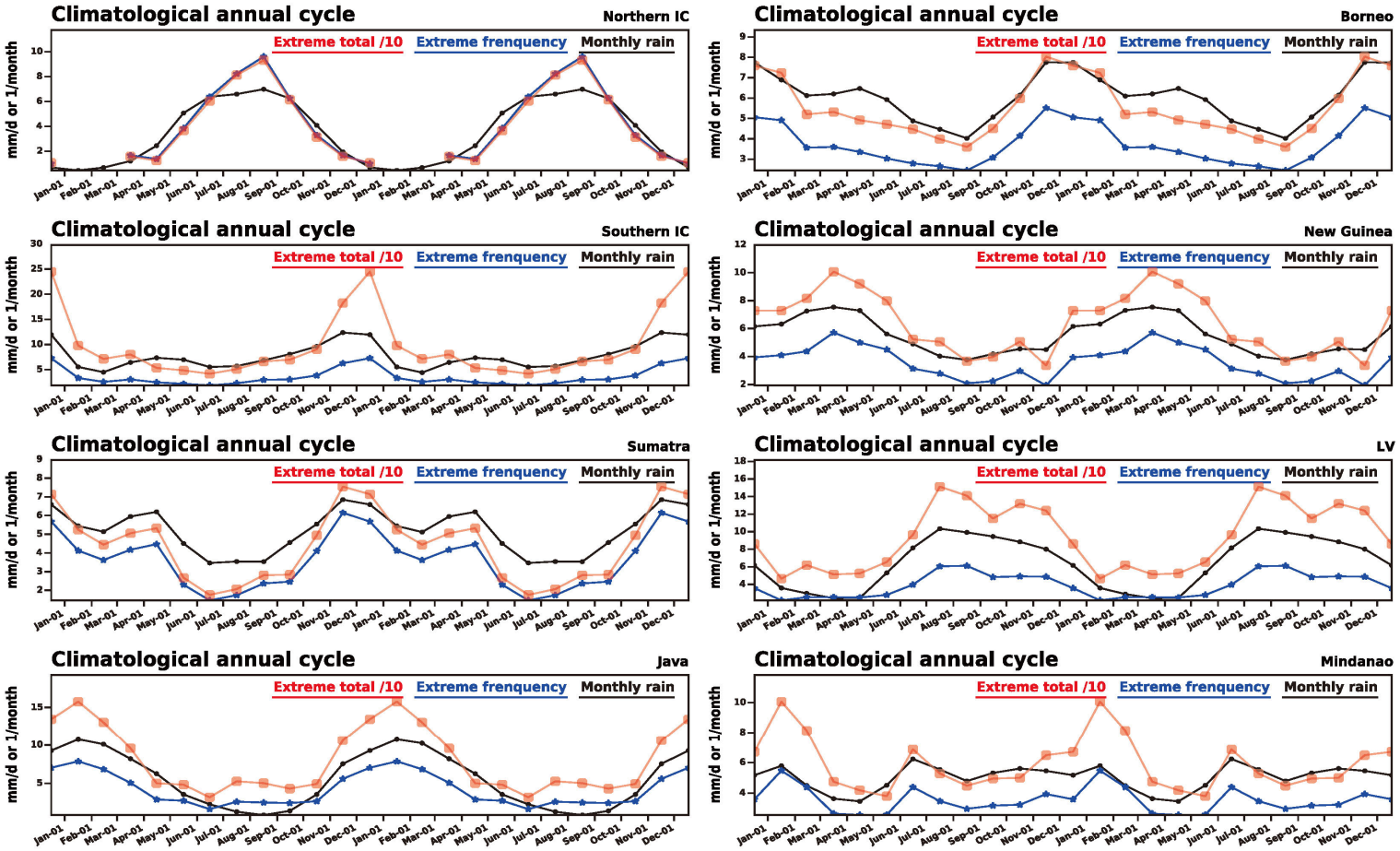

Figure 4 The monthly climatological annual cycle of total rainfall, extreme totals, and extreme frequencies over each of the eight lands. Two cycles were plotted.

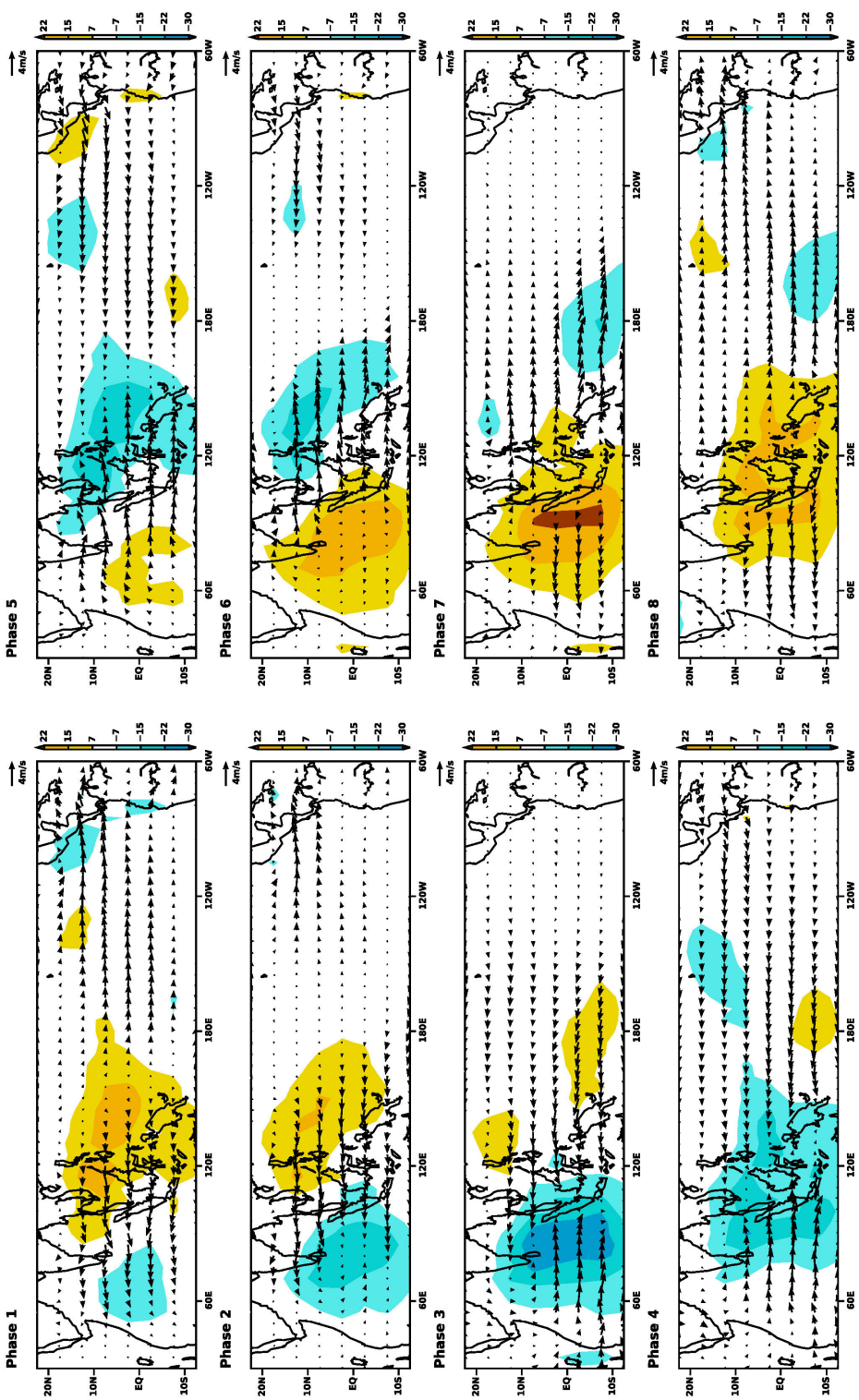

Figure 5 The Madden–Julian Oscillation (MJO) life cycle from multivariate EOF analysis. Shading shows the outgoing longwave radiation (OLR) anomaly (W/m^2). The vector is the horizontal wind anomaly at 850 hPa.

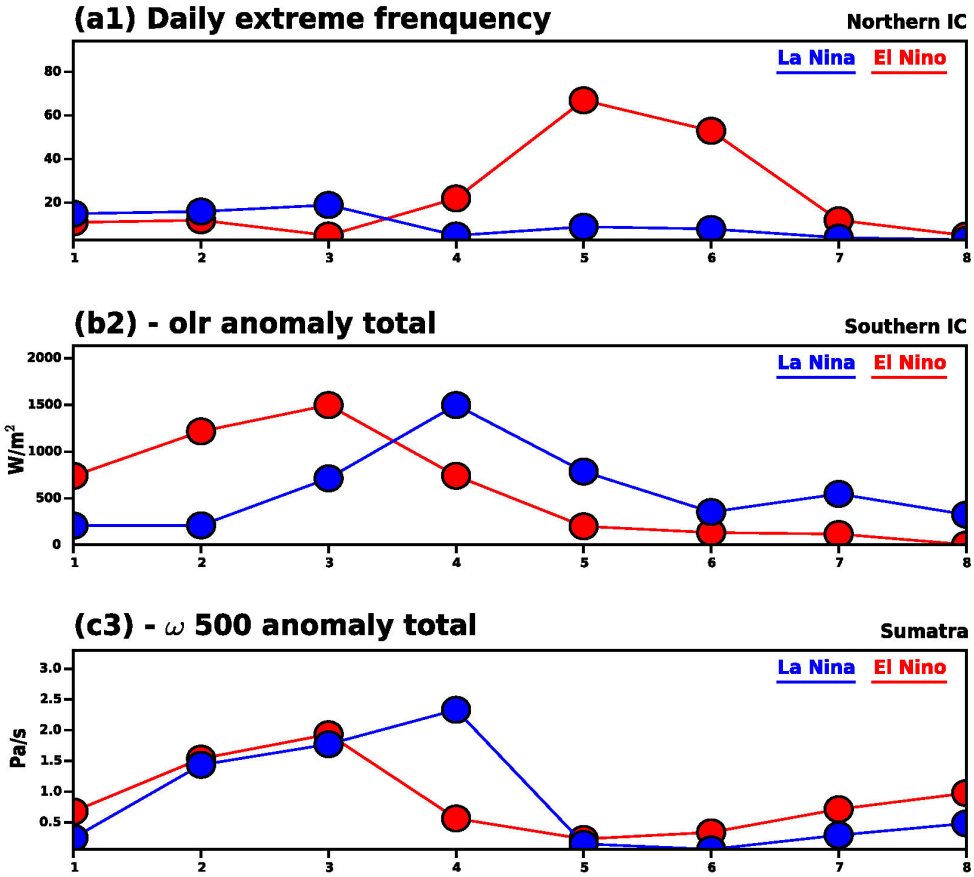

Figure 6 Composited accumulated extreme totals *det* as a function of eight MJO phases and two the El Nino Southern Oscillation (ENSO) phases averaged over eight lands (a–h). a1 is the composited accumulated extreme frequency *def* averaged over northern IC. b2 is the composited accumulated -OLR anomaly as a function of MJO and ENSO phases averaged over southern IC. c3 is the composited accumulated anomalous vertical velocity $-\omega$ at 500 hPa averaged over Sumatra.

Continue to next page

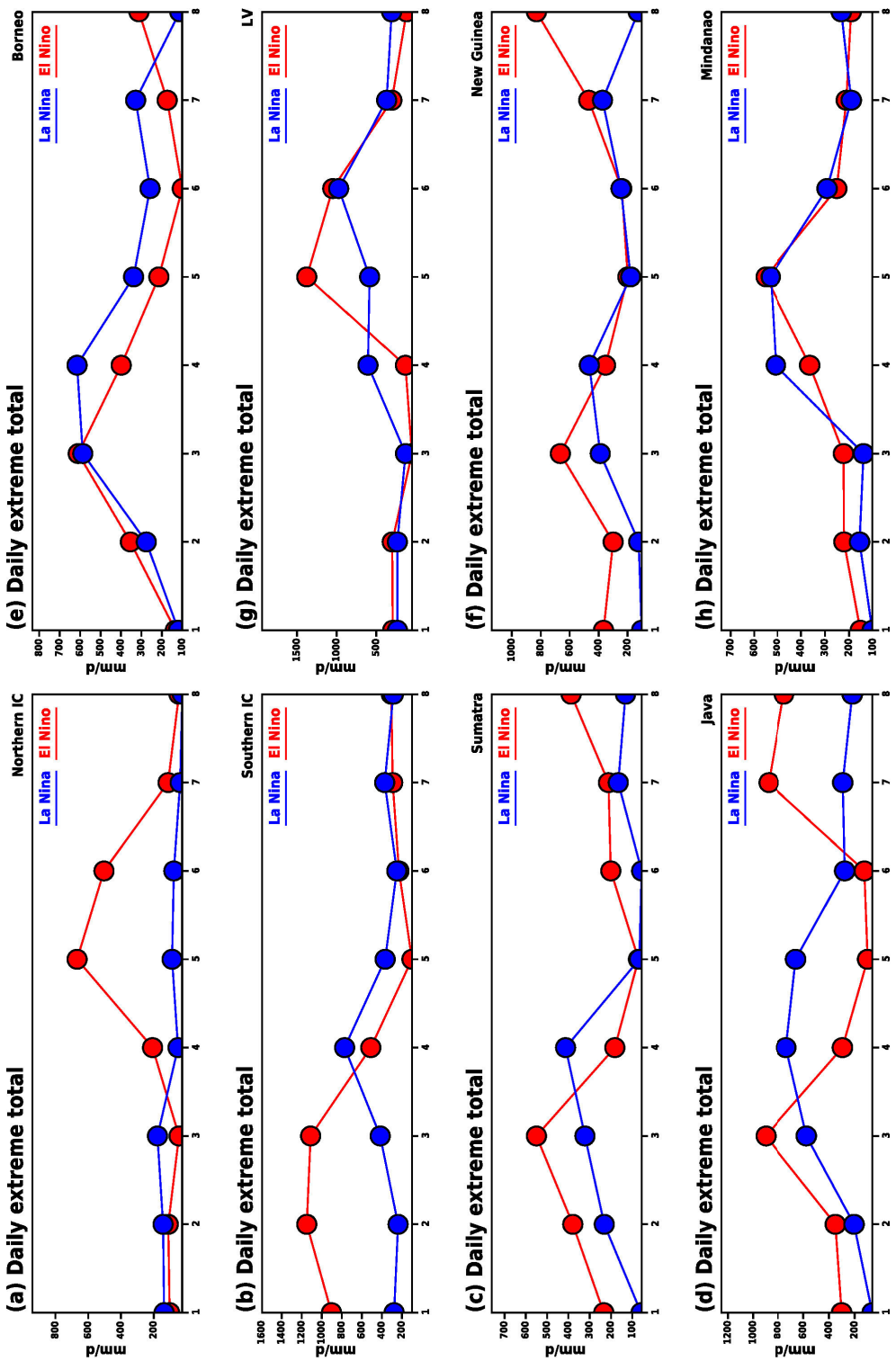
(a) Daily extreme total
Northern IC
(b) Daily extreme total
Southern IC
(c) Daily extreme total
Sumatra
(d) Daily extreme total
Java
(e) Daily extreme total
Borneo
(g) Daily extreme total
LV
(f) Daily extreme total
New Guinea
(h) Daily extreme total
Mindanao
La Nina
El Nino
mm/d

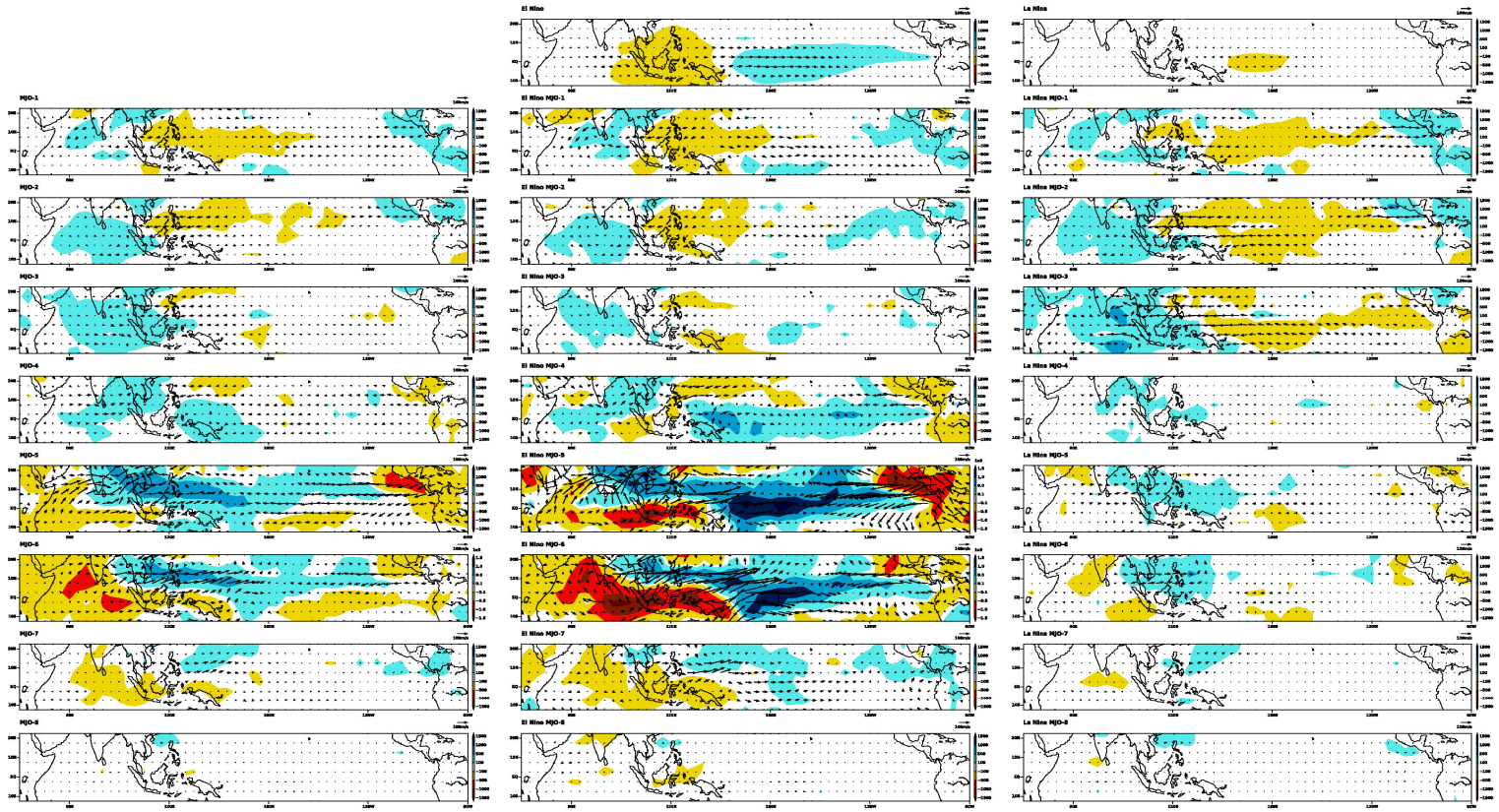

Figure 7 Anomalous evolution of -OLR and horizontal wind at 850 hPa as a function of MJO and ENSO conditional on extreme events *def* over northern IC. First row panels are the composited interannual variation of -OLR and horizontal winds at 850 hPa classified by ENSO phases conditional on extreme events over northern IC. Left column panels are the composited intraseasonal variation of -OLR and wind classified by MJO phases conditional on extreme events over northern IC. Other panels are the composited interannual and intraseasonal variation of -OLR and wind classified by ENSO in conjunction with MJO phases conditional on extreme events over northern IC. Blue color of -OLR corresponds to convection.

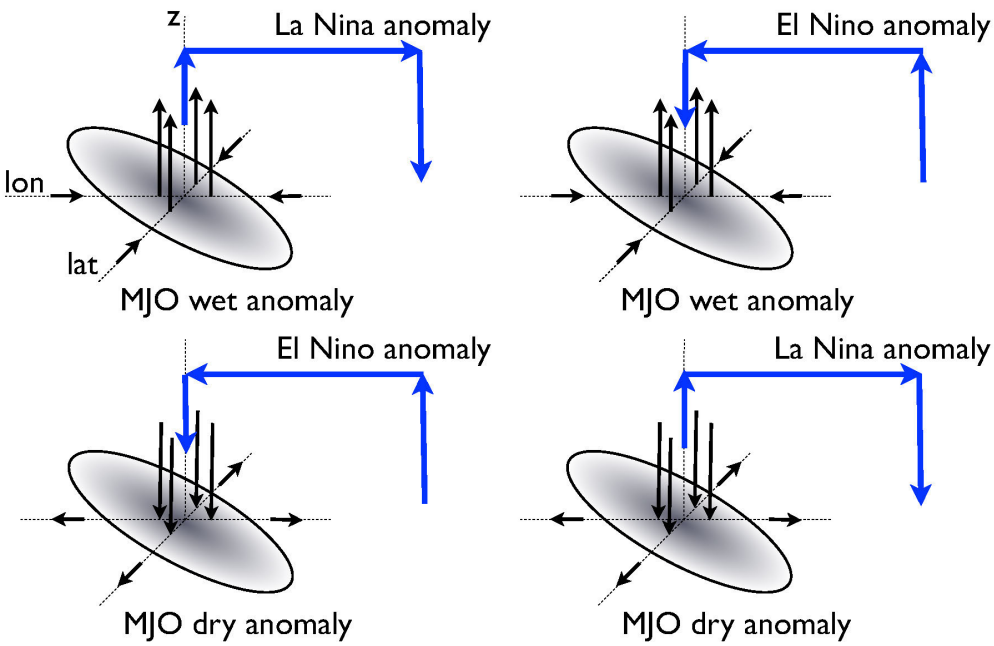

Figure 8 Schmatic diagram for impacts of ENSO in conjunction with MJO on extremes over land of the Maritime Continent. Ellipses represent the low-level northwest–southeast tilted convergence or divergence anomaly of MJO. Blue arrows represent anomalies of ENSO.

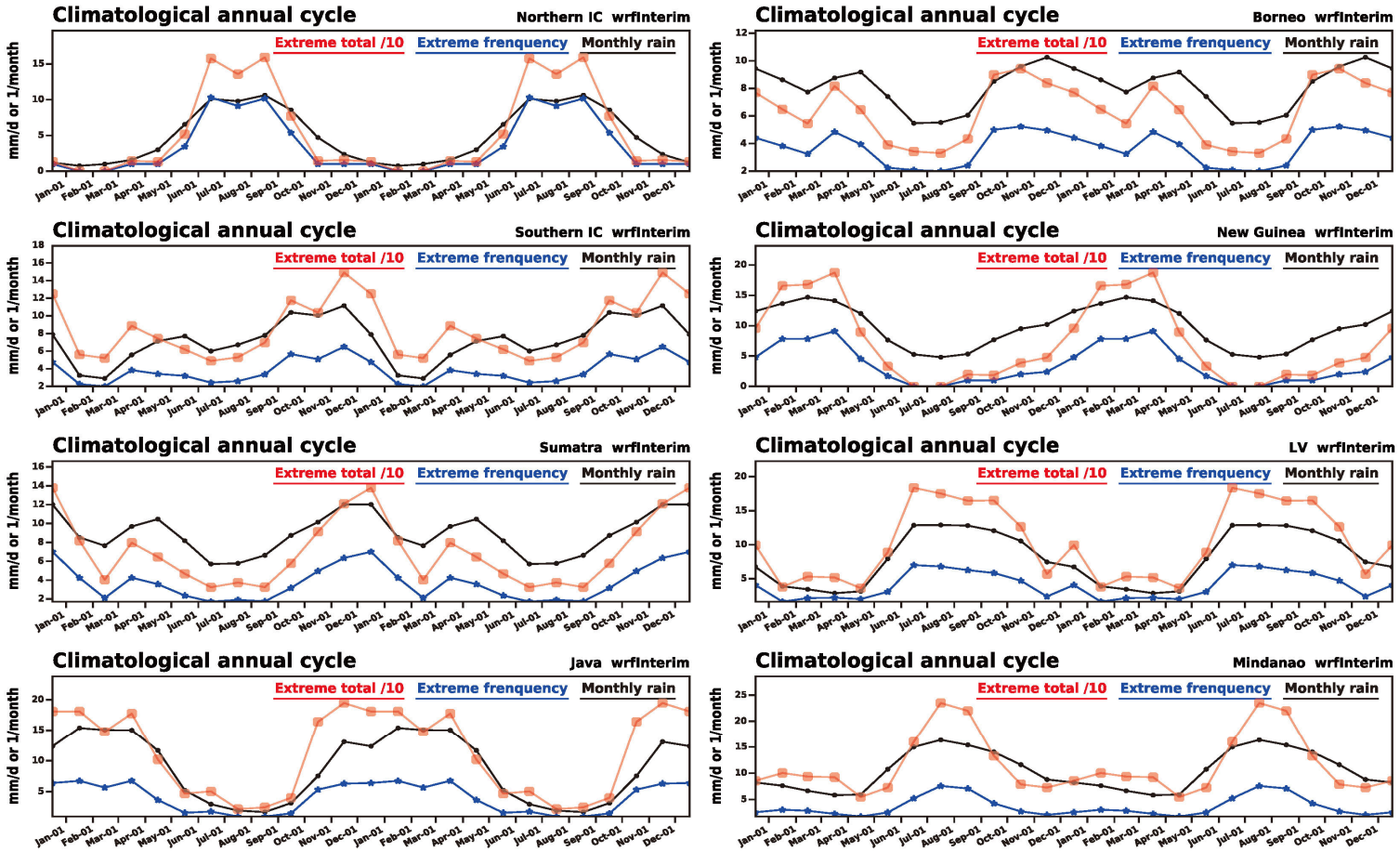

Figure 9 The monthly climatological annual cycle of total rainfall, extreme totals, and extreme frequencies simulated in the hindcast experiment. Two cycles were plotted.

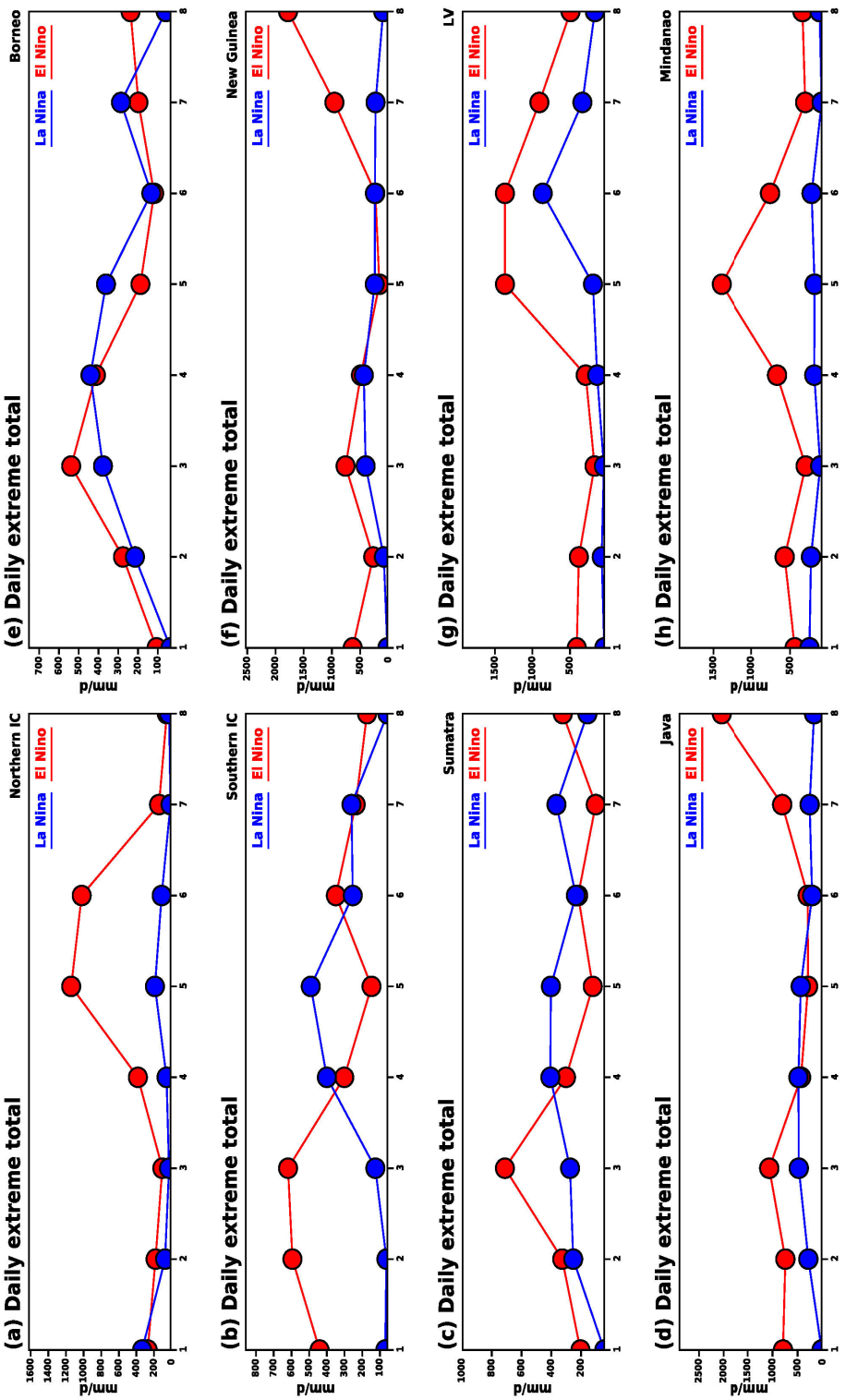

Figure 10 Composited accumulated extreme totals *det* as a function of eight MJO phases and two ENSO phases in the hindcast experiment.

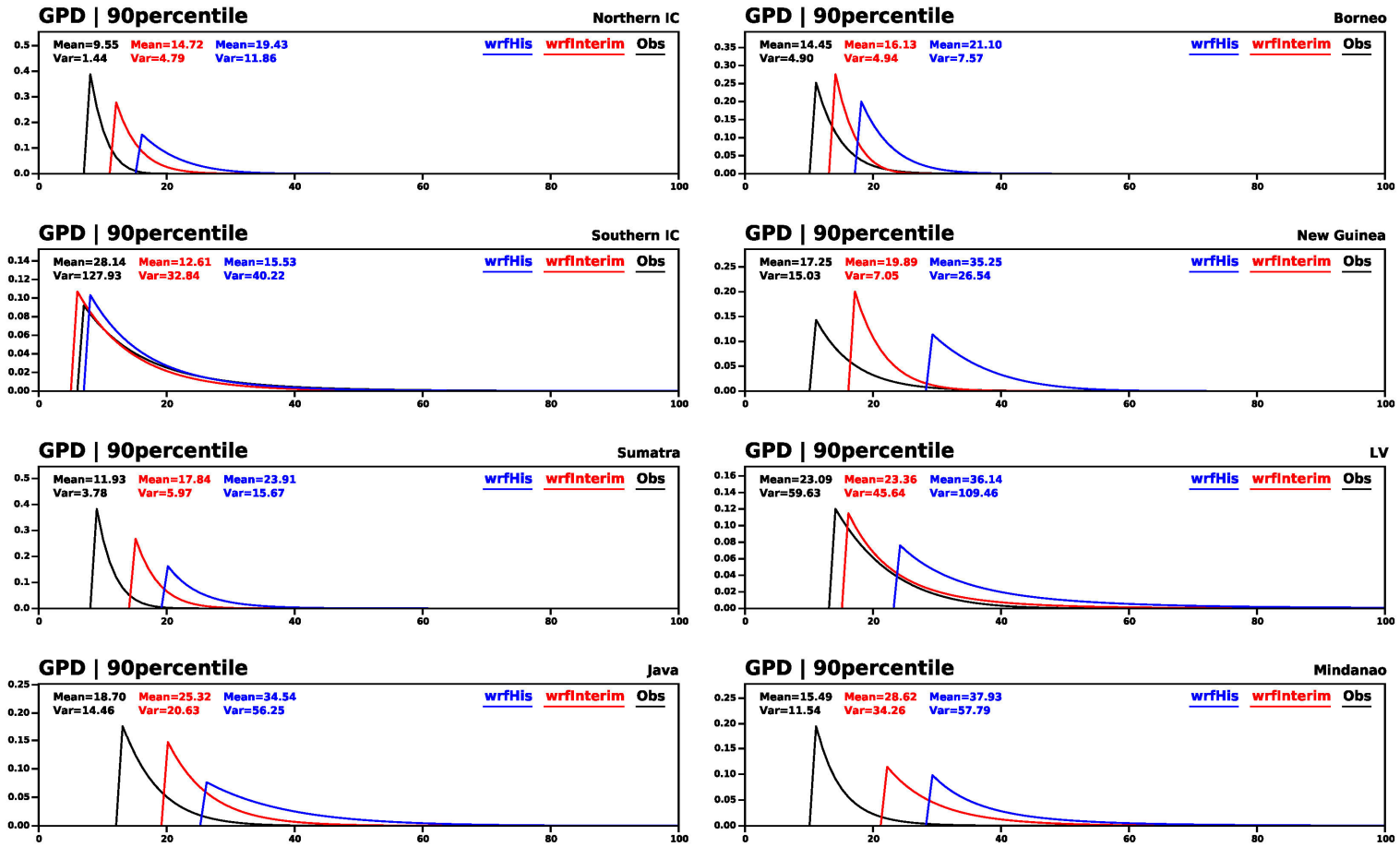

Figure 11 Probability density function (PDF)s for the extreme rainfall from the observations, hindcast experiments, and historical experiments over each land. The robust mean and robust variation are shown in each panel.

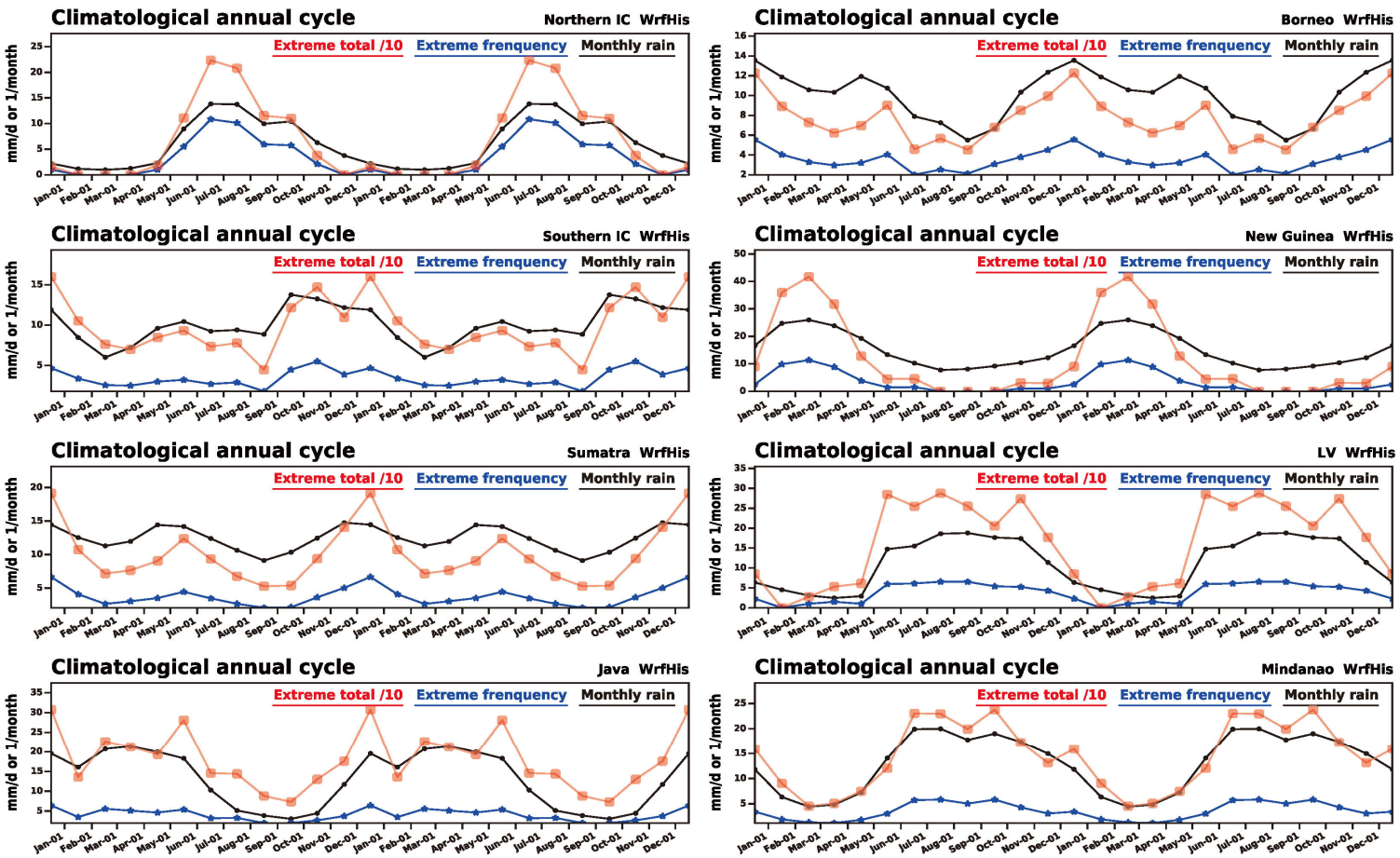

Figure 12 The monthly climatological annual cycle of total rainfall, extreme totals, and extreme frequencies simulated in the historical experiment. Two cycles were plotted.

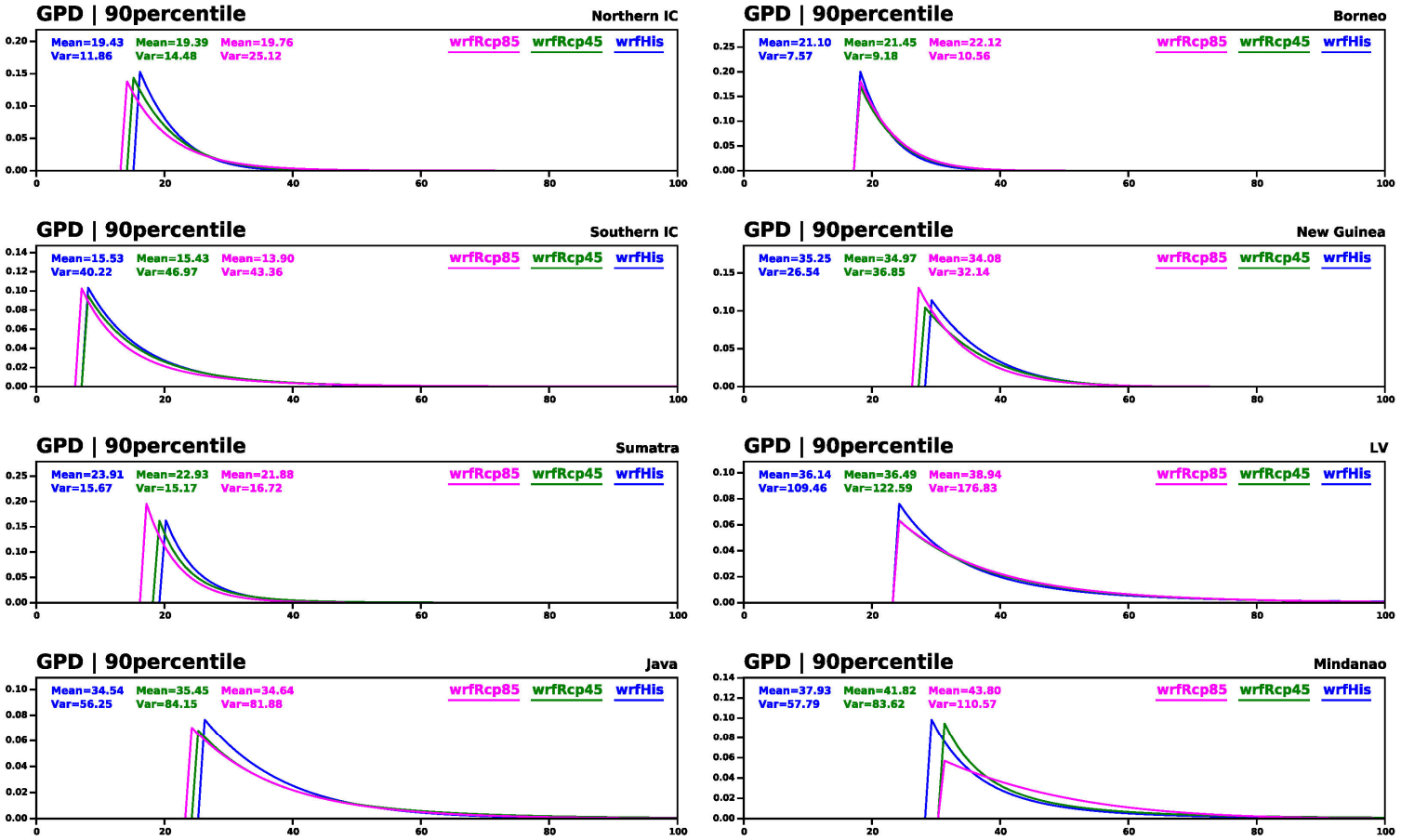

Figure 13 PDFs for extreme rainfall from the historical, near future of Down-45, and the far future of Down-85 experiments over each land. The robust mean and robust variation are shown in each panel.

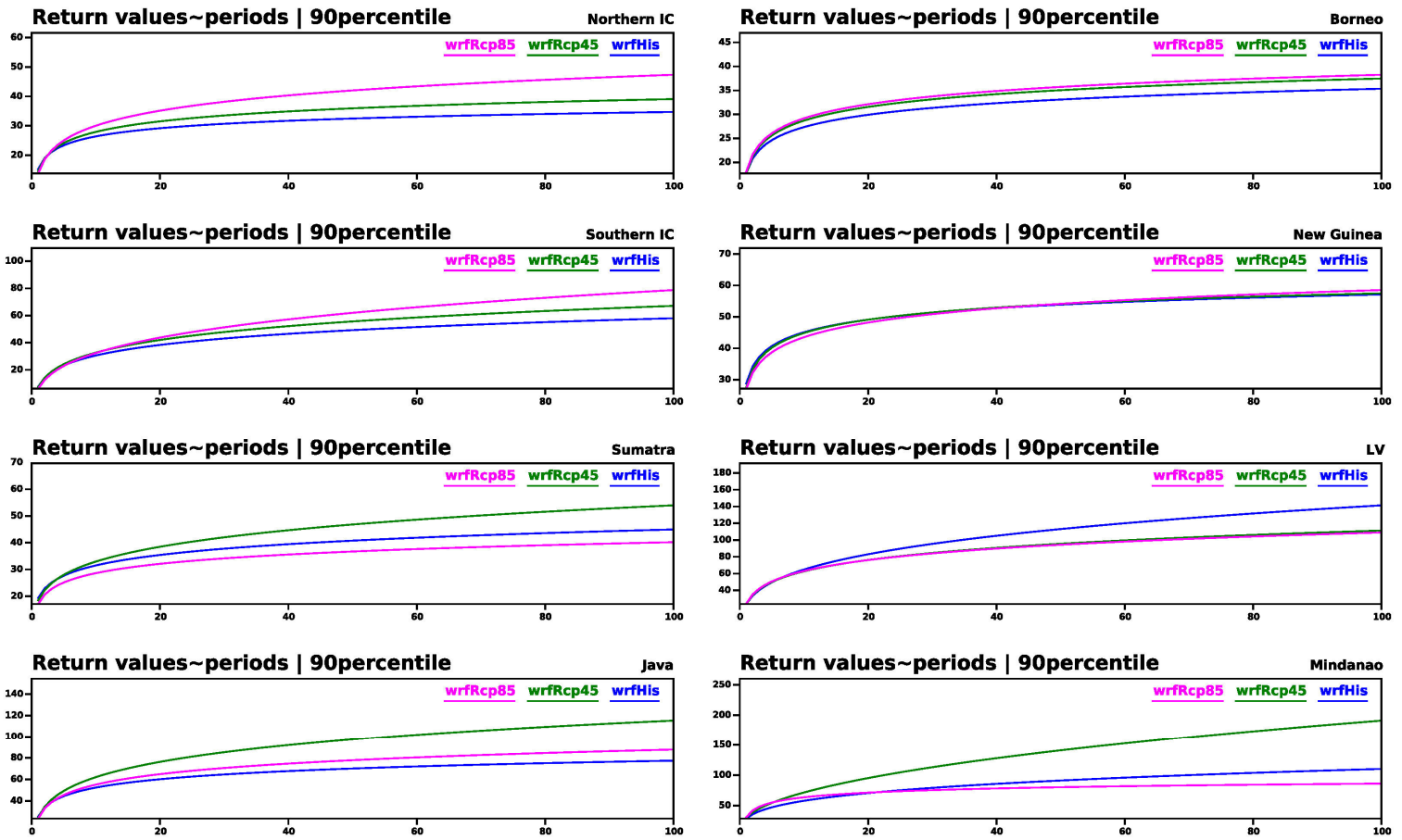

Figure 14 Return value versus return period for the historical experiment, Down-45 (RCP 4.5; 2021–2045), and Down-85 (RCP 8.5; 2071–2095) over each land.

Research Report 2015–02

Regional precipitation extremes over the Maritime Continent

Hongwei Yang

APEC Climate Center
12 Centum 7-ro, Haeundae-gu, Busan 48058, Republic of Korea
Tel: +82-51-745-3900 Fax: +82-51-745-3949

www.apcc21.org

ISBN 979-11-5698-105-3